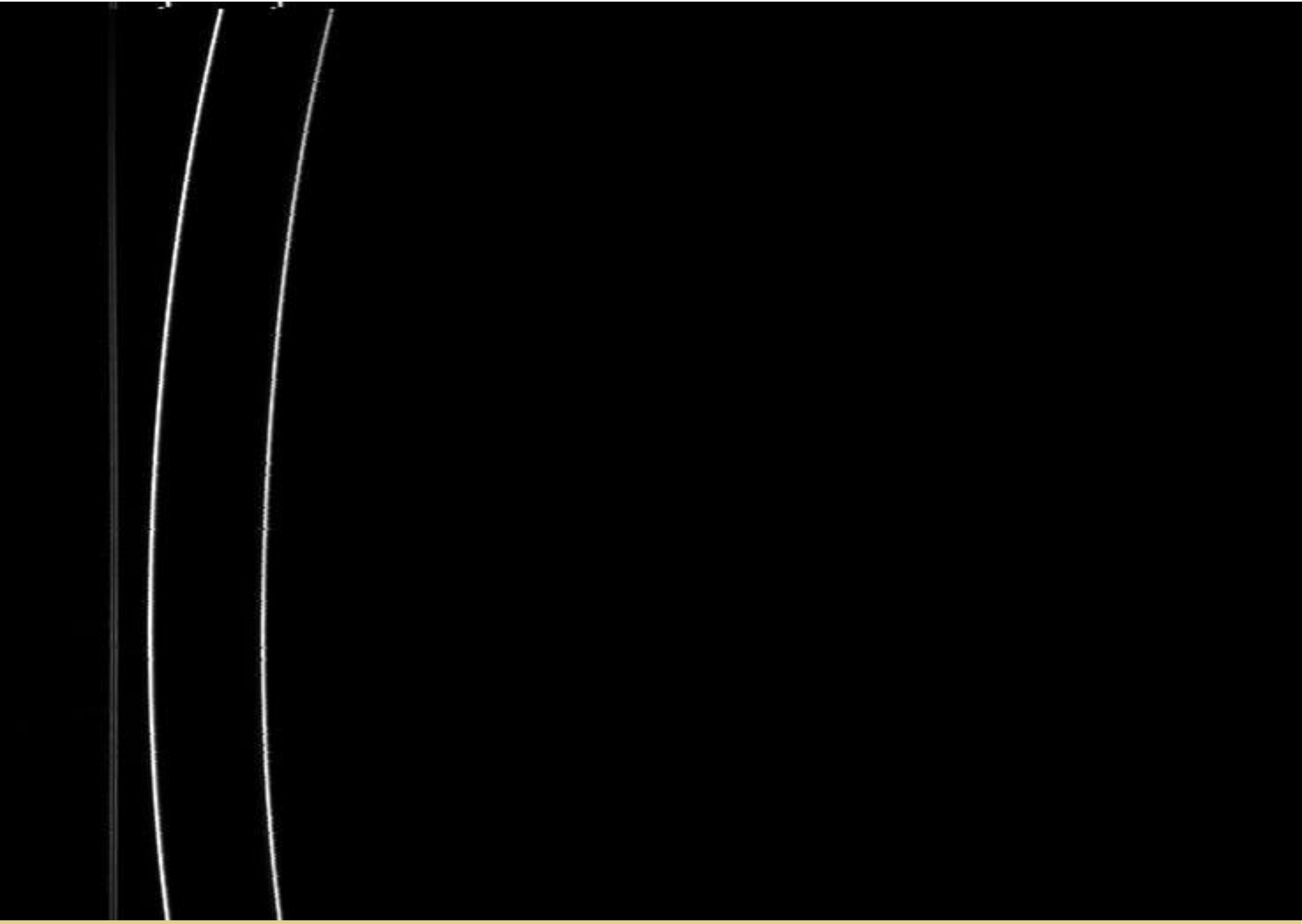

Patrícia Miguel da Silva Carvalho

OPTICAL COHERENCE TOMOGRAPHY
Layout Simulation using MATLAB®

Master Dissertation submitted in fulfilment of the requirements for the degree of Master in Physics Engineering, with specialization in Instrumentation, under the supervision of Professor António Miguel Morgado, and presented at the Department of Physics of the Faculty of Sciences and Technology of the University of Coimbra.

March 2016

Universidade de Coimbra

· U C ·

FCTUC FACULDADE DE CIÊNCIAS
E TECNOLOGIA
UNIVERSIDADE DE COIMBRA

Patrícia Miguel da Silva Carvalho

OPTICAL COHERENCE TOMOGRAPHY
Layout Simulation Using MATLAB®

Master Dissertation submitted in fulfilment of the requirements for the degree of Master in Physics Engineering, with specialization in Instrumentation, under the supervision of Professor António Miguel Morgado, and presented at the Department of Physics of the Faculty of Sciences and Technology of the University of Coimbra.

March, 2016

ACKNOWLEDGMENTS

First, I would like to thank my supervisor Professor António Miguel Morgado for all his support and guidance over the past year. His motivation and help were essential in overcoming every obstacle and small detail of this work.

I would also like to thank Professor José Paulo Domingues for his guidance in choosing this project and for his availability to answer all my questions.

I could not fail to thank my colleagues at IBILI for all their help and for the good times we spent together. Especially, I must thank Ph.D. student Susana Silva for her advices, cooperation, and patience. I must also thank Engineer Ana Domingues, for being my company during many months.

I have to thank my best friends, Ana Sofia Abreu and Carolina Carrilho, for being my family away from home since we started this adventure in 2010. We have been through a handful of moments together and I hope we experience many more.

Last, but not least, I must thank my family, my number one supporter. Without the unconditional love and support of my parents Joaquim and Beatriz, and my sister Natacha, I would not be who I am today. For being with me every step of the way, I thank you deeply.

ABSTRACT

Optical Coherence Tomography (OCT) is a non-invasive optical imaging technique capable of producing 2D images or 3D reconstructions of non-homogeneous samples. OCT is mainly used in ophthalmology as a powerful tool for the early diagnosis of ocular diseases. With OCT it is possible to obtain high resolution cross-sectional images of ocular structures, such as the retina or the anterior segment.

An OCT platform for ocular image acquisition is being developed. It is based on a swept source laser, an InGaAs balanced detector, a data acquisition board installed on a personal computer, and several optical components.

The main purpose of this thesis is the development of an analytical model of the system layout, in order to study crucial performance parameters. To achieve that, we characterized the main components of the system. A simulation of the constructed model was performed using MATLAB®. It allowed us to determine the sensitivity fall-off and axial resolution, which were compared to the experimentally measured values and to the expected values for biomedical imaging.

It was concluded that the system in development meets the necessary criteria for good quality biomedical imaging, even though the axial resolution could be improved. We also concluded that the electronic noise associated with the detector doesn't deteriorate the OCT signal.

In the future, some limitations of the simulation can be addressed, namely the characterization of the objective lenses.

Keywords: Optical Coherence Tomography, Swept-Source OCT, Layout Simulation, Axial Resolution, Sensitivity Fall-off

RESUMO

A Tomografia de Coerência Óptica (OCT) é uma técnica imagiológica não invasiva, relativamente recente, capaz de produzir imagens 2D ou reconstruções 3D de amostras não homogéneas. A OCT é maioritariamente utilizada em oftalmologia, no diagnóstico precoce de doenças oculares. Com a OCT é possível obter imagens transversais de estruturas oculares, tais como a retina ou o segmento anterior.

Uma plataforma OCT para aquisição de imagens oculares está a ser desenvolvida. Esta é baseada num laser *swept source*, num detector InGaAs balanceado, numa placa de aquisição instalada num computador pessoal, e em vários componentes ópticos.

O principal objectivo desta tese é o desenvolvimento de um modelo analítico do layout do sistema, de modo a estudar parâmetros cruciais da performance. Para atingir o objectivo, caracterizaram-se os principais componentes do sistema. O modelo construído foi simulado utilizando o software MATLAB®, o que permitiu determinar o *fall-off* da sensibilidade e a resolução axial do sistema. Estes valores foram comparados aos calculados experimentalmente e aos expectáveis para aplicações de imagiologia médica.

Concluiu-se que o sistema SS-OCT vai ao encontro dos critérios necessários para a obtenção de imagens com qualidade para medicina, apesar da resolução axial poder ser melhorada. Foi também concluído que o ruído electrónico associado ao detector não deteriora o sinal do sistema.

No futuro, algumas limitações do trabalho poderão ser abordadas, nomeadamente a caracterização das lentes objectivas.

Palavras-chave: Tomografia de Coerência Óptica, *Swept-Source* OCT, Simulação do *Layout*, Resolução Axial, *Fall-off* da Sensibilidade

TABLE OF CONTENTS

Page

ACKNOWLEDGEMENTS iii

ABSTRACT v

RESUMO vii

LIST OF FIGURES xiii

LIST OF TABLES xxi

LIST OF ABBREVIATIONS xxiii

INTRODUCTION 25

1. PRINCIPLES AND APPLICATIONS OF OPTICAL COHERENCE TOMOGRAPHY 29

1.1 PHYSICAL FUNDAMENTALS OF OPTICAL COHERENCE TOMOGRAPHY 30

1.2 MATHEMATICAL FORMULATION 33

1.3 OCT MODALITIES 35

1.3.1 Time Domain OCT 35

1.3.2 Fourier Domain OCT 36

1.4 APPLICATIONS OF OPTICAL COHERENCE TOMOGRAPHY 39

2. PRACTICAL ASPECTS OF OPTICAL COHERENCE TOMOGRAPHY 43

2.1 LIGHT SOURCES 44

2.2 AXIAL AND LATERAL RESOLUTION 49

2.3 PROBING DEPTH 52

2.4 SIGNAL TO NOISE RATIO AND DETECTION SENSITIVITY 54

3. SWEPT SOURCE OCT 59

3.1 FUNDAMENTALS OF SWEPT SOURCE OCT 60

3.2 SIMULATION OF THE SS-OCT SYSTEM 64

3.2.1 Conversion from Optical Frequencies to Electrical Frequencies 71

3.3 SS-OCT SYSTEM LAYOUT 73

3.3.1 Axsun Swept Source Engine 74

3.3.2 Thorlabs Balanced Amplified Detector – PDB471C 76

3.3.3 Thorlabs Fibre Optic Couplers – FC1064-50B-APC and FC1064-90B-APC 80

4. SIMULATION METHODS AND RESULTS 83

4.1 TIME DOMAIN OCT SIMULATION 84

4.2 FOURIER DOMAIN OCT SIMULATION 88

4.3 SWEPT SOURCE OCT SIMULATION 90

4.3.1 Sensitivity Fall-Off Simulation 95

4.3.2 Axial Resolution Simulation 98

4.3.3 Theoretical Sample A-scan and minimum detectable signal 100

4.3.4 Glass Coverslip Simulation 108

4.3.5 Small Animal Eye Model Simulation 110

5. CONCLUSIONS AND FUTURE DIRECTIONS 119

5.1 DISCUSSION OF THE FINAL RESULTS 120

5.2 FUTURE WORK 123

REFERENCES 125

APPENDIX A 131

APPENDIX B 133

LIST OF FIGURES

Page

Figure 1.1 Basic layout of an optical coherence tomography system operated on air and consisting of a light source, a beam splitter, a reference mirror, and a photodetector. Reproduced from [1]. 30

Figure 1.2 From left to right: Axial scanning of an OCT system (A-scan), cross-sectional scan (B-scan) obtained by combining a series of axial scans, and 3D reconstruction of the sample achieved by scanning multiple B-scans. Reproduced from [6]. 31

Figure 1.3 FD-OCT system layout. The reference mirror is at a fixed position and light is detected by a linear detector array. Reproduced from [1]. 37

Figure 1.4 OCT cross-sectional imaging of the human eye. Image (a) was obtained using a commercial TD-OCT system with an axial resolution of 10 µm and acquisition speed of 400 A-scans/s. Image (b) was obtained using an FD-OCT detection scheme with an axial resolution of 2 µm and acquisition speed of 30000 A-scans/s. Reproduced from [2]. 40

Figure 1.5 Swept Source OCT imaging of the porcine distal esophagus obtained in vivo. In the figure, 3D renderings with quadrant cutouts and planes are shown. Reproduced from [2]. 41

Figure 2.1 Axial resolution *vs.* bandwidth of light sources with center wavelengths of 800 nm, 1060 nm, and 1300 nm. It is clear that the broader the bandwidth is, the better is the axial resolution. Reproduced from [6]. 50

Figure 2.2 Trade-off between transverse resolution and depth, considering low and high NA focusing limits. Here, b denotes the depth of field or the confocal parameter, equal to two times the Rayleigh range, z_R. Reproduced from [6]. 51

Figure 2.3 Geometry of the sample and probe beams, where the probe beam cone and coherent probe volume can be identified. Reproduced from [5]. 53

Figure 2.4 Signal sensitivity loss with depth. Between 0 and 2 mm the signal decayed 16.7 dB. Reproduced from [20]. 58

Figure 3.1 Scheme of the FMDL concept. Reproduced from [28]. 63

Figure 3.2 Diagram of an FDML high-speed, frequency swept laser. Reproduced from [28]. 63

Figure 3.3 Simplified scheme of the layout of the SS-OCT system. 73

Figure 3.4 Time-averaged spectral power output of the SSOCT-1060 engine. Reproduced from [31]. 75

Figure 3.5 Trigger signal and optical power of the SSOCT-1060 engine. Reproduced from [31]. 75

Figure 3.6 Schematic of the balanced amplified detector. Reproduced from [32]. 76

Figure 3.7 Responsivity of the PDB471C balanced photodetector as a function of the wavelength of the incident radiation. Reproduced from [32]. 77

Figure 3.8 Frequency response of the Thorlabs PDB471C balanced amplified photodetector. Reproduced from [32]. 78

Figure 3.9 Graphical representation of the fibre optic coupler's ports. Reproduced from [33]. 80

Figure 4.1 Simulated spectrum of a Gaussian light source with parameters $\lambda_0 = 800\,nm$ and $\Delta\lambda = 50\,nm$, defined as a function of the optical frequency. 85

Figure 4.2 Obtained interferogram for the Time Domain OCT simulation. Three different peaks, corresponding to the sample's layers, can be identified: the first located at $x = 4.594\,\mu m$, the second located at $x = 25.32\,\mu m$, and the last located at $x = 69.7\,\mu m$. 87

Figure 4.3 Detected spectral intensity of a Fourier Domain OCT detection scheme. 88

Figure 4.4 A-scan of the theoretical sample defined in 4.1, for an FD-OCT detection scheme. At $x = 0$, the so-called dc component of the FT is evident. The three peaks corresponding to the sample's three layers can be identified: the first located at $x = 6.012\,\mu m$, the second located at $x = 24.05\,\mu m$, and the last located at $x = 69.14\,\mu m$. Three small peaks relative to the self-interference component of equation (8) can also be distinguished. 89

Figure 4.5 Power spectrum of the Axsun Swept Source Engine. The blue line represents the digitized values, and the red line represents the result of the interpolation. The graph on the left is the representation of the source's power as a function of the optical frequency ω, and the graph on the right is the representation of the source's power as a function of wavenumber k. 91

Figure 4.6 Magnitude response of the filter simulating the frequency response of the balanced detector. 94

Figure 4.7 Graphical representation of the simulated OCT intensity signals. 96

Figure 4.8 Sensitivity Fall-off Simulation. Graphical representation of peak sensitivity (dB) as a function of depth. An oscillation of the PSF peak values is visible. 96

Figure 4.9 Sensitivity Fall-off Simulation. Peak sensitivity as a function of depth and graphical representation of the linear regression. The linear fit made to the first dataset, ranging from 20 µm to 1.5 mm, yields a fall-off of -0.823 dB/mm (red line). The linear fit made to the second dataset, ranging from 1.58 mm to 3.58 mm, yields a fall-off of -1.841 dB/mm (green line). 97

Figure 4.10 PSF of the SS-OCT system for a mirror position of 30 µm and respective fitted function. 99

Figure 4.11 SS-OCT interference signal considering a sample with three layers. The signal is represented as a function of the electrical frequency. 101

Figure 4.12 A-scan of the theoretical sample defined in 4.1, for the SS-OCT detection scheme. The three peaks corresponding to the sample's three layers can be identified: the first located at $x = 5.339\,\mu m$, the second located at $x = 26.7\,\mu m$, and the last located at $x = 69.41\,\mu m$. 102

Figure 4.13 Graphic representation of A_2/A_1 vs. Δn. In the upper axis, the values of n_2 for each measurement are shown. In this experiment, n_1 was kept constant and n_2 varied from 1.3 to 1.05. For each n variation, we registered the amplitudes of the corresponding A-scan peaks and calculated the ratio between them. As the difference between the refractive index decreases, the ratio between the amplitude of the two peaks increases (i.e. the peak corresponding to the second layer has a much bigger amplitude than the peak corresponding to the first). 104

Figure 4.14 Graphic representation of A_3/A_2 vs. Δn. In the upper axis, the values of n_3 for each measurement are shown. In this experiment, n_2 was kept constant and n_3 varied from 1.33 to 1.50. For each n variation, we registered the amplitudes of the corresponding A-scan peaks and calculated the ratio between them. As the difference between the refractive index decreases, the ratio between the amplitude of the two peaks increases (i.e. the peak corresponding to the third layer has a much bigger amplitude than the peak corresponding to the second). 106

Figure 4.15 These graphs illustrate that for $\Delta n \leq 0.1$, it is not possible to detect the peak corresponding to the first layer, when we consider a threshold of three times the base line of the A-scan. Sample A-scan for $n_2 = 1.10$ (top) and $n_2 = 1.05$ (bottom). The remaining refractive indices were kept constant. 107

Figure 4.16 These graphs illustrate that for $\Delta n \leq 0.1$, it is not possible to detect the peak corresponding to the second layer, when we consider a threshold of three times the base line of the A-scan. Sample A-scan for $n_3 = 1.40$ (top) and $n_3 = 1.35$ (bottom). The remaining refractive indices were kept constant. 108

Figure 4.17 SS-OCT interference signal of a glass coverslip. The signal is represented as a function of the electrical frequency. 109

Figure 4.18 A-scan of a glass coverslip, for the SS-OCT detection scheme. A peak located at $x = 0.1976\, mm$ can be identified. 109

Figure 4.19 Optical parameters for the optical model of the rat eye. Reproduced from [37]. 110

Figure 4.20 Optical parameters for the optical model of the mouse eye. Reproduced from [37]. 110

Figure 4.21 Simulated A-scan of the optical model of the rat eye. Five peaks can be distinguished: the first located at 0.2136 mm, the second at 1.159 mm, the third at 7.592 mm, the fourth at 9.477 mm, and the last at 9.771 mm. 112

Figure 4.22 Simulated A-scan of the optical model of the mouse eye. Five peaks can be distinguished: the first located at 0.1281 mm, the second at 0.7368 mm, the third at 4.143 mm, the fourth at 4,885 mm, and the last at 5.211 mm. 113

Figure 4.23 Simulated A-scan of the optical model of the rat eye, with $N = 1376$. Five peaks can be distinguished: the first located at 0.2138 mm, the second at 0.2512 mm, the third at 1.165 mm, the fourth at 2.132 mm, and the last 2.432 mm. The shift in the position of the peaks due to the difference in the maximum depth is noticeable. 114

Figure 4.24 Simulated A-scan of the optical model of the mouse eye, with $N = 1376$. Five peaks can be distinguished: the first located at 0.1336 mm, the second at 0.7375 mm, the third at 2.138 mm, the fourth at 2.458 mm, and the last at 3.207 mm. The shift in the position of the peaks due to the difference in the maximum depth is noticeable. 115

Figure 4.25 B-scan of the retina of a mouse, showing the different sublayers, namely: retinal nerve fibre layer (RNFL), Inner Nuclear Layer (INL), Outer Plexiform Layer (OPL), Outer Nuclear Layer (ONL), External Limiting Membrane (ELM), and Retinal Pigmented Epithelium (RPE). Other substructures, which were not simulated, are also shown. Reproduced from [37]. 116

Figure 4.26 Simulated A-scan of the mouse retina optical model, with $N = 1376$. There are six peaks located at 26.72 µm, 106.9 µm, 144.3 µm, 235.2 µm, 267.2 µm, and 293.9 µm. 117

LIST OF TABLES

Page

Table 1 Operating and scanning parameters of the SSOCT-1060 engine. 74

Table 2 Main characteristics of the PDB471C Thorlabs Balanced Amplified Photodetector. 79

Table 3 Listing of the main specifications of the fibre optic couplers. 81

Table 4 Minimum values for the main OCT parameters in biomedical applications. [35] 83

Table 5 Characteristics of a theoretical sample with three layers, as described in [1]. 86

Table 6 Fit parameters for the two datasets, with 95% confidence bounds. These parameters were obtained using MATLAB. 98

Table 7 Parameters of the fitted Lorentz function. 100

Table 8 Statistical value R^2 for the fitted Lorentz function. 100

Table 9 Characteristics of a theoretical sample with three layers, as described in [1]. 101

Table 10 Refractive indices of the first and second layers of the theoretical sample. Simulates values of the peak position (depth) and amplitude. 103

Table 11 Refractive indices of the second and third layers of the theoretical sample. Simulates values of the peak position (depth) and amplitude. 103

Table 12 Difference between the refractive indices of the first and second layers. Ratio between the amplitudes of the peaks. 105

Table 13 Difference between the refractive indices of the second and third layers. Ratio between the amplitudes of the peaks. 105

Table 14 Simulated parameters of the rat eye optical model. 111

Table 15 Simulated parameters of the mouse eye optical model. 111

Table 16 Expected position of the A-scan peaks for the mouse and rat eye optical models. 112

Table 17 Simulated parameters of the mouse retina optical model. 116

Table 18 Expected and simulated positions of the A-scan peaks. 117

LIST OF ABBREVIATIONS

CCD	Charge Coupled Device
DFT	Discrete Fourier Transform
D-OCT	Doppler OCT
FCT	Fundação para a Ciência e Tecnologia
FDML	Fourier Domain Mode Locking
FD-OCT	Fourier Domain OCT
FT	Fourier Transform
FWHM	Full Width at Half Maximum
GVD	Group Velocity Dispersion
IBILI	Institute for Biomedical Imaging and Life Sciences
MPE	Maximum Permissible Exposure
NA	Numerical Aperture
OFDI	Optical Frequency Domain Imaging
OCT	Optical Coherence Tomography
PSF	Point Spread Function

PS-OCT	Polarization Sensitive OCT
Q-OCT	Quantum OCT
SLD	Super Luminescent Diode
SNR	Signal to Noise Ratio
SOA	Semiconductor Optical Amplifier
SS-OCT	Swept Source OCT
TD-OCT	Time Domain OCT

INTRODUCTION

In the past decades, there have been countless technological developments in biomedical imaging, with a great impact on medical diagnosis. Optical coherence tomography (OCT) is a relatively recent non-invasive imaging technique that has substituted previous invasive analysis methods.

OCT is an imaging technique based on low coherence interferometry, capable of producing high resolution cross-sectional images or 3D reconstructions of non-homogenous samples. Because of its high speed, high resolution, non-invasive character, and relative low cost, OCT is a highly attractive solution to numerous applications such as medicine, tissue engineering or nanotechnologies. Still, the greatest focus point of OCT applications is, without question, ophthalmologic imaging. OCT enables the early diagnosis of ocular diseases like glaucoma, and the monitoring of therapies and surgical procedures.

The development of the early OCT systems led to a new technique, Swept Source OCT (SS-OCT) that overcomes the limitations of the conventional systems, allowing *in vivo*, high speed image acquisition with better sensitivity.

Under the frame of the FCT project PTDC/SAU-ENB/119132/2010 – Optical modelling of the Human Retina in Health and Disease: from structure to function., an SS-OCT system is being developed at IBILI. This system is based on a swept source laser with centre wavelength of 1660 nm, 110 nm bandwidth and sweep frequency of 100 kHz, an InGaAs balanced detector, a fast multi I/O 400 MSPS data acquisition board installed on a personal computer, and several optical components, such as optical fibre cables, couplers, attenuators, objective lenses and collimators.

The main goal of this thesis is the development of an analytical model of the aforementioned SS-OCT system, in which its main components, namely the swept source laser, the optical fibre couplers, and the balanced detector, are characterized in terms of spectral response and noise. The constructed model was simulated using MATLAB®, in order to test the sensitivity fall-off and the axial resolution, crucial performance parameters of the system.

This thesis is divided into the following five chapters:

1. **Principles and Applications of Optical Coherence Tomography:** In this chapter we describe the physical fundamentals of the OCT technique as well as the mathematical formulation underlying it. The Time Domain and Fourier Domain OCT modalities are presented and some applications of OCT systems are discussed.

2. **Practical Aspects of Optical Coherence Tomography:** This chapter focus on the paramount aspects of OCT. So, an analysis of the importance of the used light source is made. The resolution, both axial and lateral, the probing depth, the signal to noise ratio and the detection sensitivity are discussed.

3. **Swept Source OCT:** In this chapter, after a brief introduction of the SS-OCT systems and its fundamental principles, we describe in detail the equations that describe the operation of an SS-OCT system. The layout of the OCT system in development at IBILI is also presented, with a description of the main components and their characteristics.

4. **Simulation Methods and Results:** Chapter 4 is summarized into two main blocks, the simulation of the equations for TD- and FD-OCT systems and the simulation of the layout of the SS-OCT system following the description made in chapter 3. The methods used to perform the mentioned simulations are described and the results are presented and discussed.

5. **Conclusions and Future Directions:** In this chapter, a summary of the main conclusions of the work is presented and the limitations of the simulations are addressed. We also present possible future work that can lead to overcoming the said limitations.

In the final appendices, we present the source code built to simulate the SS-OCT system, as well as the source code for the simulation of basic Time Domain and Fourier Domain OCT systems.

1. PRINCIPLES AND APPLICATIONS OF OPTICAL COHERENCE TOMOGRAPHY

Optical coherence tomography (OCT) is a non-invasive imaging technique, based on low coherence interferometry. This technique facilitates the acquisition of high-resolution cross-sectional images or 3D reconstructions through inhomogeneous samples, such as biological tissue.[1]

The imaging process in OCT is similar to an ultrasound, in which the time travelled by a sound wave since its emission until its detection, after being reflected by an object, is measured. So, reconstructions of the structure of a certain sample are obtained by measuring the time it takes for a light beam to travel the optical path due to the reflection of an object, as well as the magnitude of the back-reflected light.[2][3] Since it is not possible to accurately measure such time values, low-coherence light and interferometry become valuable techniques for OCT.

OCT is mostly used for non-invasive structural and quantitative imaging of the retina and anterior segment of the eye, allowing the identification of morphological changes and, therefore, the diagnosis of pathologies, and monitoring the response to therapy.[4] As a result of its characteristics, OCT is a highly attractive non-invasive imaging technique that can be used in a great number of areas.

1.1 PHYSICAL FUNDAMENTALS OF OCT

OCT is an interferometric technique that depends on the interference between two light beams, usually with wavelengths in the infrared range. The basic OCT setup, shown in figure 1.1, is similar to a Michelson interferometer.

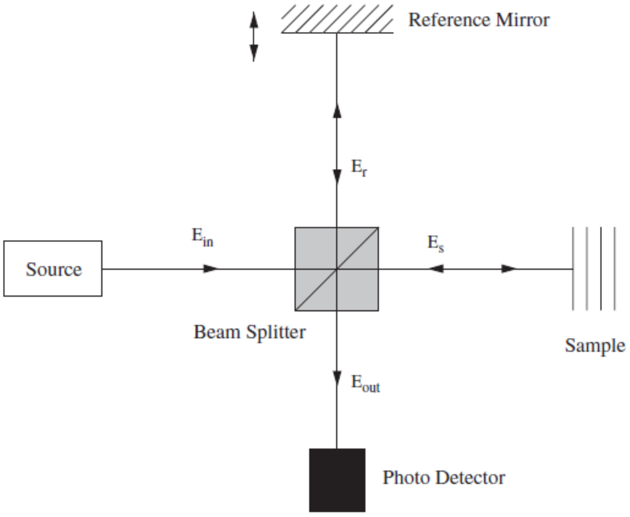

Figure 1.1 Basic layout of an optical coherence tomography system operated on air and consisting of a light source, a beam splitter, a reference mirror, and a photodetector. Reproduced from [1].

A light beam, emitted by the light source, is split on a beam splitter. The split beam is sent into a reference path and into a sample path. The first is reflected by a reference mirror and the latter is reflected from the different layers within a sample.[1] The reflected beams are recombined and detected by a photodetector, where an interference pattern is obtained. In it, is possible to identify intensity peaks due to sharp refractive index variations between layers of the sample. Thereby, it is possible to infer about the structure of the studied sample.

It is crucial to note that the interference between the reflected light only occurs when the optical path lengths of the reference and sample arms differ no more than a value equal to the coherence length of the light (l_c). Therefore, the axial resolution of an OCT system is determined by the temporal coherence of the light source (t_c). [1]

In this configuration, the reference mirror position is altered within a pre-determined range of values corresponding to an imaging depth range of interest in order to obtain a full A-scan profile. The A-scan is a map of the reflectivity of the sample along an axial depth direction.[3] By combining a series of axial depth scans (A-scan), cross-sectional scans of the sample (B-scan) are obtained.[5] It is also possible to obtain 3D reconstructions of the studied sample by scanning a series of B-scans. Figure 1.2 shows the different OCT images, obtained by measuring the magnitude and echo time delay of the light.

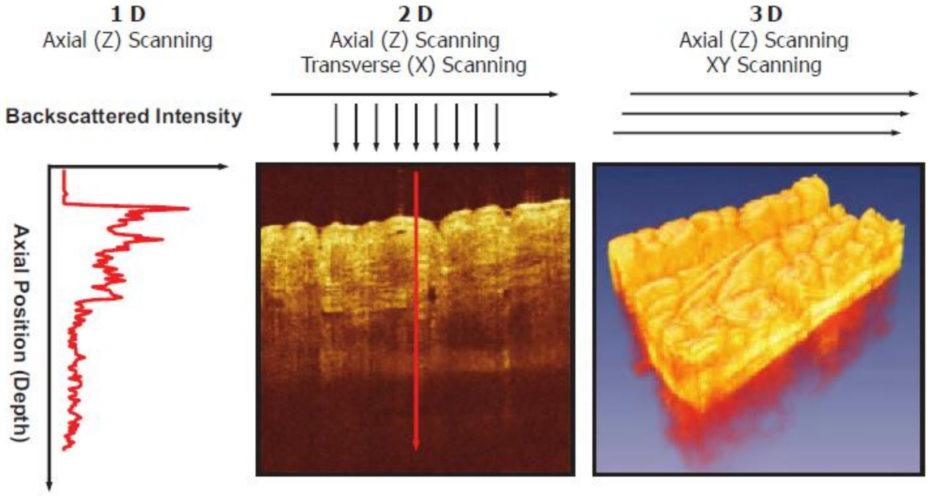
1 D
Axial (Z) Scanning
Backscattered Intensity
Axial Position (Depth)
2 D
Axial (Z) Scanning
Transverse (X) Scanning
3 D
Axial (Z) Scanning
XY Scanning

Figure 1.2 From left to right: Axial scanning of an OCT system (A-scan), cross-sectional scan (B-scan) obtained by combining a series of axial scans, and 3D reconstruction of the sample achieved by scanning multiple B-scans. Reproduced from [6].

In the next pages, we will present the mathematical formulation of OCT systems, following the treatment presented by Tomlins and Wang. [1]

1.2 MATHEMATICAL FORMULATION

Considering the OCT system represented previously in figure 1.1, the optical field at the input of the interferometer is characterized by:

$$E_{in}(\omega, t) = s(\omega)e^{-i\omega t} \tag{1}$$

where $s(\omega)$ is the source field amplitude spectrum, ω is the frequency, and t is the time variation. The phase term is ignored, since the initial phase of the incident wave is arbitrary.

In the beam splitter, the incident wave $E_{in}(\omega, t)$ is split in a reference beam $E_r(\omega, t, \Delta z)$, and in a sample beam $E_s(\omega, t)$. The reference beam is reflected by a reference mirror, and the sample beam is reflected by the structures within the sample:

$$E_r(\omega, t, \Delta z) = (T_r T_s)^{\frac{1}{2}} E_{in}(\omega, t)e^{-i\phi(\Delta z)} \tag{2}$$

$$E_s(\omega, t) = (T_r T_s)^{\frac{1}{2}} E_{in}(\omega, t)H(\omega) \tag{3}$$

Here T_r and T_s represent the reference and sample arms intensity transmission coefficients; and $H(\omega)$ represents the frequency domain response function of the sample. The scanning of the mirror position, by a geometric distance $\Delta z = \frac{\Delta tc}{n_{air}}$, results in a phase accumulation $\phi(\Delta z)$ that is determined as:

$$\phi(\Delta z) = \frac{2\omega n_{air}\Delta z}{c} \tag{4}$$

The frequency domain response function of the sample, $H(\omega)$, that describes its internal structure is characterized by $r(\omega, z)$, the backscattering coefficient from the sample structural features, and by $n(\omega, z)$, the frequency dependent, depth varying group refractive index:

$$H(\omega) = \int_{-\infty}^{+\infty} r(\omega, z) e^{i2n(\omega,z)\omega z/c} \, dz \tag{5}$$

At the output of the interferometer, the optical field is a consequence of the interference between the sample and reference beams:

$$E_{out}(\omega, t) = E_r(\omega, t) + E_s(\omega, t, \Delta z) \tag{6}$$

The photodetector records an optical intensity proportional to a time average of the output electrical field multiplied by its complex conjugate:

$$I(\omega, \mathit{\Delta} z) = \langle E_{out} E_{out}^* \rangle = \langle E_s E_s^* \rangle + \langle E_r E_r^* \rangle + 2\Re\{\langle E_s E_r^* \rangle\} \tag{7}$$

where the first two terms correspond to the *self-interference* term and the last to the real part of the *cross-interference*.

Considering the equations describing the reference and sample optical fields and substituting $s(\omega)$ by the source power spectrum $S(\omega) = |s(\omega)|^2$, recorded optical intensity is given by:

$$I(\omega, \Delta z) = T_r T_s \, S(\omega) |H(\omega)|^2 + T_r T_s \, S(\omega) + 2T_r T_s \, \Re\left\{S(\omega) H(\omega) e^{-i\phi(\Delta z)}\right\} \tag{8}$$

1.3 OCT MODALITIES

The information about the optical structure of a sample can be retrieved from measurements in both time and frequency domain. These techniques are labeled Time-Domain OCT (TD-OCT) and Fourier-Domain OCT (FD-OCT). Depending on the area of application other modalities, such as Quantum OCT (Q-OCT), Polarization Sensitive OCT (PS-OCT) or Doppler OCT (D-OCT), can be used. However, we will not discuss these modalities in this work.

1.3.1 Time Domain OCT

In a Time-Domain OCT (TD-OCT) system, as described in the previous sections, the reference mirror is moved in order to match the optical path from the reflections within the sample.[1]

Assuming an ideal situation in which the OCT system is operated on air and there are no losses on the beam splitter (with a 50:50 ratio), and writing the optical intensity recorded by the photodetector as a function of the mirror displacement, the obtained interference pattern in each axial scan can be described as:

$$I(\Delta z) = \mathit{\Gamma}_0 + \Re\{\mathit{\Gamma}(\mathit{\Delta} z)\} \tag{9}$$

where Γ_0 is the self-interference term, and $\Gamma(\Delta z)$ is the cross-interference term:

$$\Gamma_0 = \frac{1}{4}\int_{-\infty}^{+\infty} S(\omega)(|H(\omega)|^2 + 1)d\omega \tag{10}$$

$$\Gamma(\Delta z) = \frac{1}{2}\int_{-\infty}^{+\infty} H(\omega)S(\omega)cos\{\phi(\Delta z)\}d\omega \tag{11}$$

If we consider a sample composed of N individual layers, the sample's response function can be obtained from equation (5), using the layer interface's reflectivities (r_j), according to:

$$H = \sum_{j=1}^{N} r_j\, exp\left\{i2\frac{\omega}{c}\sum_{m=1}^{j} n_m z_m\right\} \tag{12}$$

where z_m is the thickness of each layer, and n_m is the refractive index. The reflectivites r_j are determined by the Fresnel's equations:

$$r_j = \frac{n_{j+1} - n_j}{n_{j+1} + n_j} \tag{13}$$

A typical TD-OCT uses as light source superluminescent diodes (SLD) with a central wavelength $\lambda_0 \approx 800nm$ and a full width at half maximum $FWHM \approx 50nm$.

1.3.2 Fourier Domain OCT

In a Fourier-Domain OCT (FD-OCT) the measurements are taken in the frequency space and the reference arm of the system is fixed.

In order to obtain the intensity spectrum of the reflected light, the reference mirror is at a fixed position ($\Delta z = 0$) and the light is detected through a spectrometer. The intensity spectrum ($I(\omega)$) is Fourier transformed (FT) to obtain a time domain interference pattern ($I(t)$):

$$I(\omega) = \frac{1}{4} S(\omega)[H(\omega) + 1]^2 \tag{14}$$

$$I(t) = FT\{I(\omega)\} \tag{15}$$

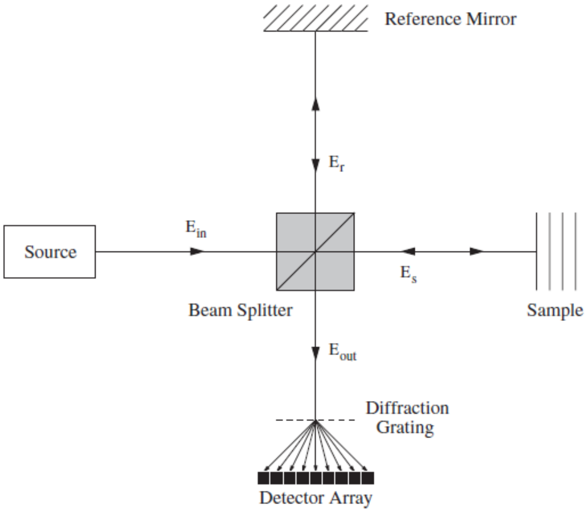
Reference Mirror
E_r
E_in
Source
Beam Splitter
E_s
Sample
E_out
Diffraction Grating
Detector Array

Figure 1.3 FD-OCT system layout. The reference mirror is at a fixed position and light is detected by a linear detector array. Reproduced from [1].

Figure 1.3 exemplifies an FD-OCT system using a linear detector array. The output intensity spectrum is a set of N data points, in which each point matches a recorded intensity at each detector of the array. As the time domain interference pattern is obtained from the output intensity spectrum, using the Fourier

Transform, it will have only $\frac{N}{2}$ data points corresponding to a time interval $\Delta\tau$ given by the detected spectral width (ΔΩ):

$$\Delta\tau = \frac{2\pi}{\Delta\Omega} \tag{16}$$

$$\Delta\Omega = 2\pi c \frac{\Delta\lambda}{\lambda^2} \tag{17}$$

The conversion from time to spatial domain is achieved by multiplying both sides of equation (17) by $\frac{c}{n_{avg}}$, where n_{avg} is the average sample refractive index. Therefore, the maximum depth z_{max} can be calculated by multiplying equation (17) by $\frac{N}{2}$ and dividing by two to account the double pass of the light through the sample:

$$z_{max} = \frac{1}{4n_{avg}} \frac{\lambda_0^2}{\Delta\lambda} N \tag{18}$$

It follows that the maximum probing depth depends linearly on the number of detector elements N.

It is also possible to implement an FD-OCT system using a single detector. This is done by sequentially recording the optical intensity in a photodetector while synchronously sweeping the wavenumber of a narrowband swept laser source.[7] This modality, Swept-Source OCT (SS-OCT), also called optical frequency-domain imaging or OFDI by some authors, is discussed in detail in chapter 3.

1.4 APPLICATIONS OF OPTICAL COHERENCE TOMOGRAPHY

Being a high-resolution, non-invasive and fast acquisition technique, OCT is suitable for a wide variety of applications, from biomedicine to materials research.

OCT was initially applied for ophthalmologic imaging, and today it is still most used in biomedicine. Compared with other imaging techniques, OCT provides some features that make it appealing. The independence of the depth resolution with the sample beam aperture, the improved probing depth, the high depth and transversal resolution, and the possibility to create function dependent image contrast are some of the said features. [5]

As mentioned before, OCT was first applied for imaging in the eye, and the first in vivo tomograms of the human optic disc and macula were demonstrated in 1993.[8] OCT is a fundamental tool for the early diagnosis and analysis of ocular diseases, including macular holes, macular edema or glaucoma. It also facilitates the monitoring of therapies and surgical procedures, for instance, it can be used to guide laser treatment and non-invasively monitor patient performance before, during, and after surgery.[1]

Figure 1.8 shows two cross-sectional images of the human eye, obtained *in vivo*, using two different OCT detection schemes.

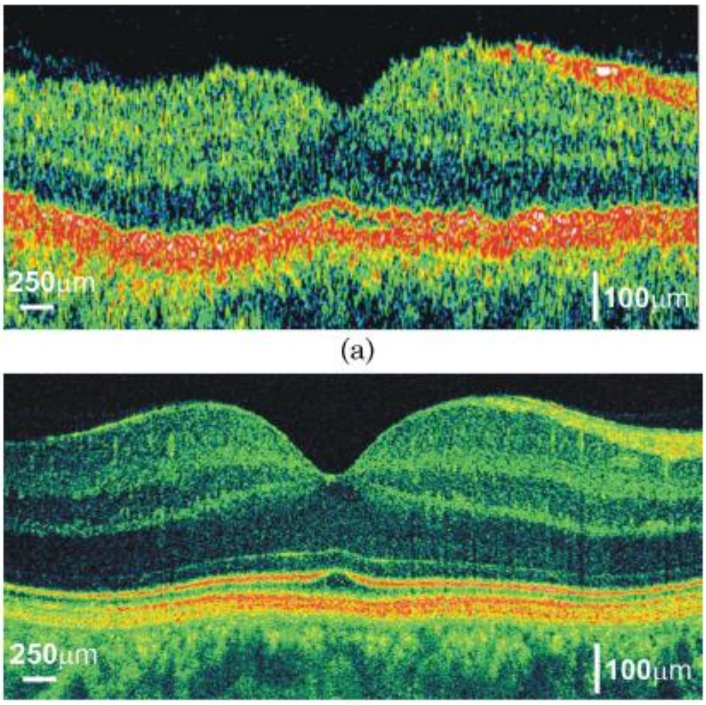

(a)

(b)

Figure 1.4 OCT cross-sectional imaging of the human eye. Image (a) was obtained using a commercial TD-OCT system with an axial resolution of 10 µm and acquisition speed of 400 A-scans/s. Image (b) was obtained using an FD-OCT detection scheme with an axial resolution of 2 µm and acquisition speed of 30000 A-scans/s. Reproduced from [2].

It is also possible to use OCT as an alternative to the customary histology and excisional biopsy methods. In this context, OCT is valuable in imaging tissue pathologies in situations where conventional excisional biopsies would be dangerous, guiding conventional biopsy to reduce false negative rates from sampling error, and the detection of early neoplastic changes.[8] Studies have shown that cancer tissue absorb and scatter near-infrared light more than the surrounding healthy tissue. Thus, it is possible to use OCT in order to diagnose tumors. Moreover, OCT has been applied to miniature and flexible imaging probes, enabling the acquisition of images of internal organ systems. In vivo imaging of animal and human gastrointestinal, urinary, and genital tracts, has already been performed. As an example, images of the porcine distal esophagus obtained using swept-source OCT systems are presented in figure 1.9.

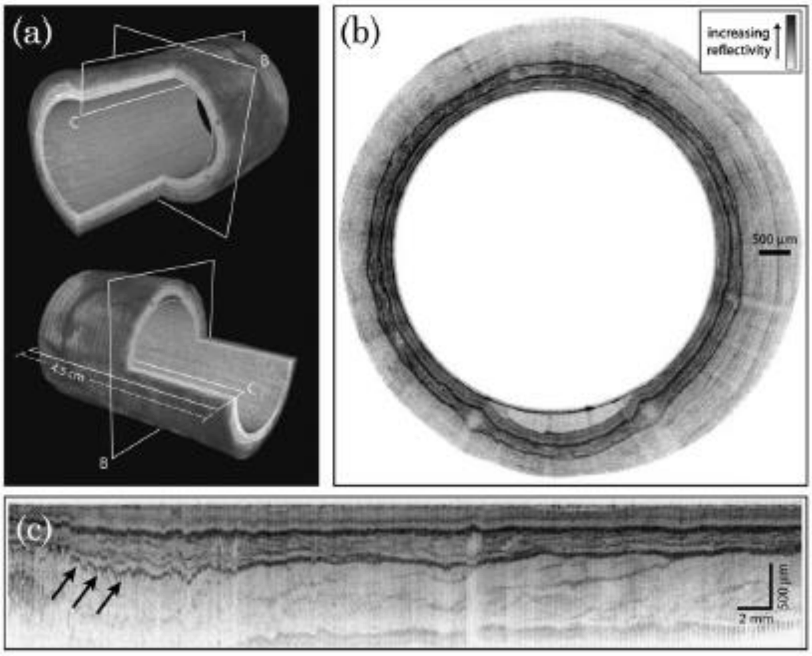

Figure 1.5 Swept Source OCT imaging of the porcine distal esophagus obtained in vivo. In the figure, 3D renderings with quadrant cutouts and planes are shown. Reproduced from [2].

Concerning tissue engineering and biomaterials, OCT is adequate for the setup of automated, non-invasive, and precise measuring systems used for quality control of engineered tissue for surgical implantation. Additionally, OCT can be applied in nanotechnology, and developments have been made in analyzing the complex flow dynamics within microfluidic structures, using Doppler OCT.

OCT has also been proposed as a suitable technology for high-density data storage on multilayer optical discs, the nondestructive study of polymer matrix composites, and evaluation of paints, coatings, plastics and ceramics. [1][8]

2. PRACTICAL ASPECTS OF OPTICAL COHERENCE TOMOGRAPHY

In this chapter, the main aspects of OCT systems are addressed. Concerning the hardware of an OCT, the available light sources and its properties are described. The resolution, probing depth, signal to noise ratio and detection sensitivity, crucial parameters of any OCT system, are discussed.

2.1 LIGHT SOURCES

One of the most important components of an OCT system is the light source since its parameters influence the system's performance. Therefore, an appropriate choice of light source is paramount to the optimization of the system. Three requirements must be considered when choosing a source for OCT imaging: emission in the near infrared, short temporal coherence length and high irradiance.[9]

The biological tissues studied using OCT systems aren't homogeneous. They consist of a gelatinous matrix of collagen and elastin fibres, containing cells, blood vessels, nerves, and other structures. These materials have different absorption and scattering coefficients that vary with the wavelength of the incident radiation. It is found that scattering decreases with increasing wavelength and absorption has minimum values for a spectral window between 600 nm and 1300 nm. Noting that these phenomena affect the probing depth, the light source should operate in a spectral range in which the penetration of light into tissue is adequate. For instance, for a source emitting in the blue and ultraviolet region, OCT imaging would be limited to the superficial layers of the studied sample. Consequently, for biological tissue imaging, the favored wavelength region ranges from $800\ nm$ to $1300\ nm$. [5][9][10]

Typical OCT systems use low coherence light sources. It is said that a light source is coherent when there is a fixed phase relationship between the electric field values at different locations or at different times. Spatial coherence occurs when a strong correlation between the electric field values at different points in space across the beam profile is verified, and temporal coherence occurs when there is a strong correlation between the electric fields at one spatial point but different times. [11]

Considering a source with a Gaussian spectrum whose spectral full width at half maximum $\Delta\omega$ is given by:

$$\Delta\omega = 2\sqrt{2\ln(2)}\omega \tag{19}$$

Its inverse Fourier Transform is also a Gaussian, described by:

$$A(t) = e^{-1/4t^2\omega^2} \tag{20}$$

The coherence time of the source (t_c) is determined by the FWHM of $A(t)$:

$$t_c = \frac{1}{\Delta\nu}\frac{4\ln(2)}{\pi} \tag{21}$$

The coherence length of the light source (l_c), defined as the FWHM of the source's self-coherence function multiplied by the speed of light. Since,

$$\frac{\Delta\nu}{\Delta\lambda} = -\frac{c}{\lambda^2} \tag{22}$$

we obtain

$$l_c = ct_c = \frac{4\ln(2)}{\pi}\frac{\lambda_0^2}{\Delta\lambda} \tag{23}$$

where λ_0 is the central wavelength of the source, and $\Delta\lambda$ is the bandwidth.[1]

Both temporal and spatial coherence affect the resolution of the OCT system, due to the relationship between the temporal coherence of the light source and the width of the axial point-spread function (PSF) of an OCT scanner. Usually, the resolution and contrast of the obtained images improve with the broadening of the emission bandwidth of the source. Furthermore, the shape of the source's spectrum has an important role in the performance of an OCT system. [9] It has been shown that the use of non-Gaussian source causes side lobes in the final interferogram that appear as shadow artifacts in the final image. Jansz et al. [12] simulated the use of multiple Gaussian sources with constant bandwidth and demonstrated that for non-Gaussian spectrums the side lobes of a strongly reflective layer appeared equal or greater than the real layer peaks of other layers in the A-scan. Thus, the use of light sources with a non-Gaussian spectrum leads to a reduced quality A-scan, preventing the obtaining of accurate information regarding the studied tissues.

The last requirement, high irradiance (i.e. the flux per unit area striking an elementary surface), is due to the need for a wide dynamic range and high detection sensitivity. However, higher power increases excess noise that compromises the system's sensitivity, and as OCT is mainly used for biological tissue imaging, the irradiance of the light source should not overcome the Maximum Permissible Exposure (MPE). [5][9][13]

One of the most commonly used light sources for OCT imaging are super luminescent diodes (SLDs). SLDs work like a forward biased pn junction for which a large forward bias produces a large density of electron-hole recombination and resulting light emission. Because of the high injection current, spontaneous emission is amplified, resulting in amplified emission. However, it is necessary to maintain the high gain at a level that doesn't result in lasing, and thus loss of spectral width. SLDs dominated the early work of OCT due to their smooth Gaussian spectra, simplicity, and low cost. Currently, SLDs have broad spectra, with $\sim$ 20 nm bandwidth, and center wavelengths ranging from 675 nm to 1550 nm. A typical SLD, with $\Delta\lambda = 20\ nm$, has a coherence length of 44 µm that leads to a depth resolution of 22 µm, which in tissue, considering a refractive index $n = 1.44$ gives 16 µm. [1][12][14]

Solid state lasers are another used light source for OCT, and its broad emission spectra can be used as a superluminescent source or through mode locking. These lasers rely on a crystalline gain medium, and rare earth ions can be doped into the crystal, replacing one of the host ions at a specific lattice site. The choice of the crystal and rare earth ions allow different possibilities of excitation and emission wavelengths. Most OCT systems use Ti:Sapphire laser systems operating in mode-locked regime. These devices enable the generation of broadband light, with near Gaussian spectral profiles, and intensities high enough to perform high-resolution imaging. Common Ti:Sapphire lasers can have bandwidths as high as 170 nm, making it possible to obtain axial resolutions in air close to 1 µm. [1][10][13]

Swept-source lasers should also be mentioned as a significant light source for OCT imaging systems. A swept-source laser is a tunable light source emitting one wavelength at a time, rapidly swept over a broad spectral range. The output laser is a tuned wavelength train with long pulses. Swept-source lasers have ideal features for OCT systems, such as the broad tuning bandwidth, high sweep rate, tens of mW output power, and appropriate coherence length. [13][15]

2.2 AXIAL AND LATERAL RESOLUTION

In OCT systems, resolution is defined as axial (depth) resolution and lateral (transverse) resolution. These are essential specifications, since many OCT application, especially those in the field of biomedicine, require high resolutions that allow the discrimination between different cell structures and tissues. It should be noted that unlike conventional microscopy, in OCT, axial and lateral resolution are two completely independent variables.

In both TD-OCT and FD-OCT, and considering a source with a Gaussian spectrum, axial resolution is determined as half of the source's coherence length and high axial resolution can be achieved independently of the beam focusing conditions. It should be noted that the coherence length is the width of the field autocorrelation produced by the interferometer, and its envelope is equivalent to the FT of the power spectrum. Therefore, the axial resolution is inversely proportional to the width of the power spectrum.

Following equation (23), the axial resolution (Δz) is determined by:

$$\mathit{\Delta} z \ = \frac{l_c}{2} = \frac{2\ln(2)}{\pi}\frac{\lambda_0^2}{\mathit{\Delta}\lambda} \tag{24}$$

where λ_0 is the center wavelength of the source, and $\Delta\lambda$ is the FWHM of the source's autocorrelation function and power spectrum. The axial resolution is inversely proportional to the bandwidth of the light source and depends entirely on the source's characteristics. [8]

In figure 2.1, a graph of axial resolution *vs.* bandwidth of light sources with center wavelengths of 800 nm, 1060 nm and 1300 is shown.

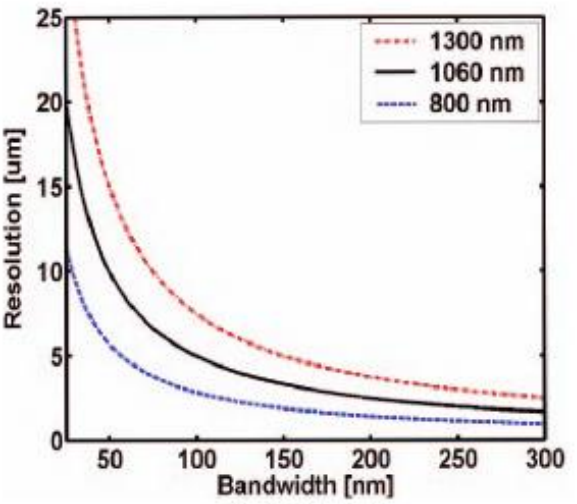

Figure 2.1: Axial resolution *vs.* bandwidth of light sources with center wavelengths of 800 nm, 1060 nm, and 1300 nm. It is clear that the broader the bandwidth is, the better is the axial resolution. Reproduced from [6].

As in optical microscopy, transverse resolution of an OCT system is determined by the focusing properties of an optical beam, namely the minimum spot size of the focused probing beam. This parameter is also inversely proportional to the numerical aperture (NA) of the focusing lens. Thus, transverse resolution is determined by:

$$\Delta x = \frac{4\lambda_0}{\pi}\left(\frac{f}{d}\right) = \frac{4}{\pi}\frac{\lambda_0}{NA} \tag{25}$$

where f is the focal length of the objective lens (i.e. the objective lens or lens system at the end of the sample arm), and d is the spot size of the probing beam as it is projected on the objective lens. [8][16]

Theoretically, it’s possible to individually optimize both axial and transverse resolution, as these two parameters are independent. However, like the transverse resolution, probing depth also varies with the numerical aperture of the objective lens. Therefore, a trade-off between these two parameters is necessary.

Figure 2.2 shows the low and high numerical aperture focusing limits and the trade-off between transverse resolution and depth.

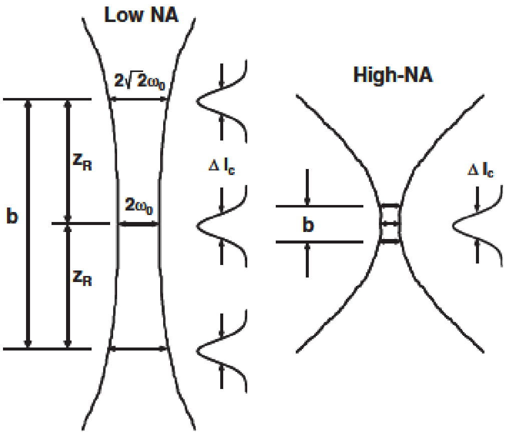

Figure 2.2: Trade-off between transverse resolution and depth, considering low and high NA focusing limits. Here, b denotes the depth of field or the confocal parameter, equal to two times the Rayleigh range, z_R. Reproduced from [6].

2.3 PROBING DEPTH

Probing depth is a critical parameter in OCT and is strongly limited by dispersion and absorption phenomena. These phenomena decrease linearly with greater wavelengths and, therefore, wavelengths in the infrared range are favored in order to optimize probing depth.

Probing depth is also dependent on scattering anisotropy, aperture of the objective lens, and on the sample distribution between lens and coherence gate.

Multiple scattered light does not contribute to the Fourier spectrum of the studied sample, leading to a reduction of image contrast and resolution, and to a reduction of penetration depth. It is, then, important to achieve a balance between multiple and single scattered light. The latter is limited to photons scattered at the coherent probe volume that equals the depth of the coherence gate (i.e. the coherence length (l_c)) multiplied by the corresponding beam cross section. Considering double scattered photons, the first scattering event should occur within the illuminating probe beam cone and, due to the coherence condition, the second must occur within or close to the coherent volume, shown in figure 2.3. Consequently, probing depth is determined by the path length of single and double scattered photons, and can be defined as the depth at which double scattering dominates. [5]

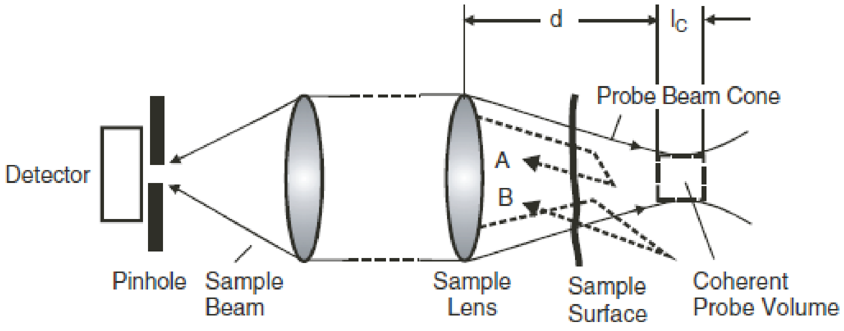
d
l_C
Probe Beam Cone
Detector
A
B
Pinhole
Sample Beam
Sample Lens
Sample Surface
Coherent Probe Volume

Figure 2.3 Geometry of the sample and probe beams, where the probe beam cone and coherent probe volume can be identified. Reproduced from [5].

In section 1.3.2, the maximum probing depth for TD- and FD-OCT system is determined as a function of the source's parameters, center wavelength and bandwidth. In section 2.2, it is mentioned that the maximum probing depth is also related to the transverse resolution and can be determined as:

$$z = \frac{\pi}{4\lambda_0}\Delta x^2 \tag{26}$$

Substituting equation (25) into equation (26) gives:

$$z = \frac{4\lambda_0}{\pi}\left(\frac{f}{d}\right)^2 \tag{27}$$

The relationship between the spot size and probing depth for low and high NA is schematically represented in figure 2.2. It shows that for a higher value of the numerical aperture of the beam, the maximum probing depth is smaller. Most OCT systems operate with a low numerical aperture focusing in order to obtain a greater probing depth.

2.4 SIGNAL TO NOISE RATIO AND DETECTION SENSITIVITY

An important feature of an OCT system is the signal to noise ratio (SNR) that defines the ratio of the mean square signal photocurrent $\langle i_{ph}^2 \rangle$ from the detector to the total photocurrent variance σ_i^2: [17]

$$SNR = \frac{\langle i_{ph}^2 \rangle}{\sigma_i^2} \tag{28}$$

Typically, the SNR is measured in dB and equation (28) is rewritten as:

$$SNR = 10\, log_{10} \left(\frac{\langle i_{ph}^2 \rangle}{\sigma_i^2} \right) \tag{29}$$

The photocurrent generated at the photodetector is due to the interference of the reference and sample beams. It is determined by the optical power in the reference and sample arms after reflection by the mirror and the sample:

$$i_{ph} = \frac{\eta q_e}{h\nu} \sqrt{2 P_s P_R} \tag{30}$$

where P_s and P_R are the optical powers on the sample and reference arms, respectively, and $\frac{\eta q_e}{h\nu}$ is the responsivity of the photodetector.

When calculating the SNR, three main noise sources should be considered: receiver noise, shot noise, and excess photon noise.[1][5][17][18][19]

Receiver noise is the noise associated with the detector electronics. It can be calculated from the manufacturer's specifications or modelled as thermal noise. Thermal (or Johnson) noise is generated by an effective resistance (R_{eff}) experienced by the photocurrent, and can be determined as:

$$\sigma_{th}^2 = \frac{4kTB}{R_{eff}} \tag{31}$$

where k is the Boltzmann's constant, T is the absolute temperature (Kelvin), and B is the detection bandwidth.

Both shot and excess photon noise are dependent upon the average photocurrent at the detector (i_{dc}). Shot noise is caused by the quantization of light and is a result of the random distribution in arrival times of photons. This is a Poisson process and its variance is given by:

$$\sigma_{shot}^2 = 2q_e i_{dc} B \tag{32}$$

where q_e is the electronic charge.

Finally, excess photon noise arises from the beating between different spectral components within the linewidth and is determined as:

$$\sigma_{ex}^2 = \frac{i_{dc}^2 B}{\Delta\nu} \tag{33}$$

where $\Delta\nu$ is the effective linewidth of the source.

If the degree of source polarization (Π) is considered, equation (33) becomes:

$$\sigma_{ex}^2 = (1+\Pi^2)\frac{i_{dc}^2 B}{\Delta\nu} \tag{34}$$

Considering the obtained equations for the generated photocurrent and its variance, the SNR is given by:

$$SNR = \frac{2\alpha^2 P_S P_R}{\frac{4kTB}{R_{eff}} + 2q_e i_{dc}B + (1+\Pi^2)\frac{i_{dc}^2 B}{\Delta\nu}} \tag{35}$$

where $\alpha = \frac{\eta q_e}{h\nu}$.

Equation (35) shows that the SNR is proportional to the power on the sample and reference arms, and inversely proportional to the bandwidth B, which is a function of the acquisition time τ:

$$B = \frac{1}{\tau} \tag{36}$$

It is, therefore, concluded that the SNR of an OCT system can be improved by increasing the acquisition time, leading, however, to a diminished rate of image capture. [1]

When using a balanced detection scheme, the excess intensity noise is suppressed, and the dominant remaining noise source is shot noise. This leads to an improvement of around 40 dB in the SNR. [17]

The sensitivity S of an OCT system is another important aspect that can be defined as the ratio of the signal power generated by a perfectly reflecting mirror ($R = 1$) and the signal generated by the weakest sample reflectivity R_{min}. [5] In other words, it is defined as the ratio of the maximum signal over noise floor. Considering that the signal powers are proportional to the corresponding reflectivities, the sensitivity is determined by:

$$S = \frac{1}{R_{min}}\bigg|_{SNR=1} \tag{37}$$

If a Michelson interferometer with an ideal and symmetric beam splitter is considered, and if the system is operated in a shot noise dominant regime, the sensitivity is given by:

$$S = \frac{\alpha}{4}\frac{P_{Source}}{q_e}\frac{1}{B} \tag{38}$$

The system's sensitivity is, thus, proportional to the source's power (P_{Source}) and inversely proportional to the electronics' bandwidth B.

It is important to point out that the sensitivity of an FD-OCT system has a strong dependence on depth. This fall-off of sensitivity can be explained as the decreasing visibility of higher fringe frequencies corresponding to large sample depths. Figure 2.4 shows the loss in sensitivity of a signal from a weak reflector.

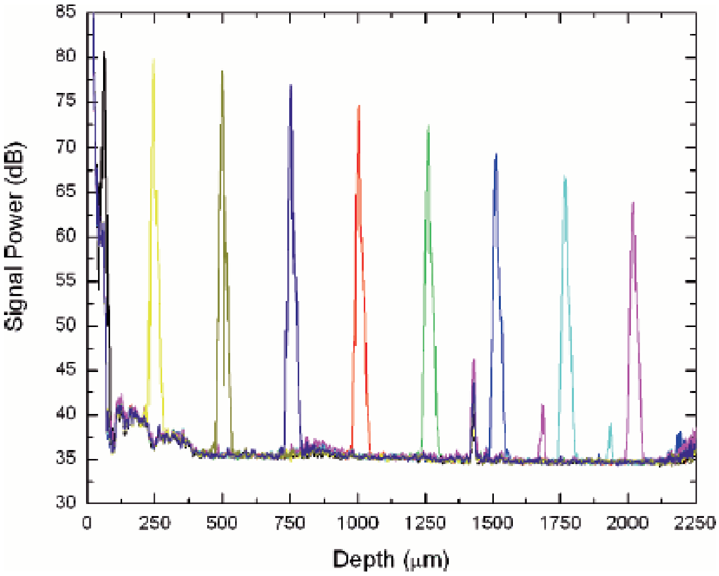

Figure 2.4 Signal sensitivity loss with depth. Between 0 and 2 mm the signal decayed 16,7 dB. Reproduced from [20].

Furthermore, the sensitivity of an OCT system is also limited by the bandwidth of the detector and by the depth of focus defined by the optical components of an OCT system.

3. SWEPT SOURCE OCT

Fourier Domain OCT is an alternative OCT technique based on spectral interferometry, in which the measurements are taken in the frequency space. In FD-OCT the reference arm is kept stationary, leading to an improved acquisition rate. Additionally, FD-OCT offers better sensitivity than the typical TD-OCT systems. In FD-OCT, the individual spectral components of the light, after interference, are detected separately using a spectrometer and a charged coupled device (CCD) array. The depth information is, then, obtained by applying the FT to the spectrally resolved interference fringes. [3][20][21]

As an alternative to the typical FD-OCT technique, it is possible to use a wavelength swept laser and a standard single element photodetector. This approach is normally used when imaging highly scattering tissues at longer wavelengths. Some of its advantages over FD-OCT are reduced fringe washout, lower sensitivity fall-off, higher imaging rate, higher detection efficiencies, and the opportunity to implement dual balanced detection. [4][21][22]

3.1 FUNDAMENTALS OF SWEPT-SOURCE OCT

In Swept-Source OCT, the wavenumber of a narrowband swept laser source is synchronously swept and the interference between the light on the reference and sample arms is detected with a square-law photodetector. The axial reflectivity profile (A-scan) is obtained by applying the discrete Fourier transform (DFT) to the sampled detector signals, [21][23]

The acquired SS-OCT signal is a photocurrent integrated over the linewidth δk of the swept laser source:[24]

$$i_{SS}(k) \propto \int_{k}^{k+\delta k} S(k)\, cos(2kz)\, dk \tag{39}$$

where k is the optical wavenumber, z is the optical path length difference between the sample and reference arms, and $S(k)$ is the source's spectral density.

Swept-source OCT offers a sensitivity advantage over typical TD-OCT systems. If the analysis of Choma et al. [25] is followed, the signal to noise ratio of an SS-OCT system, for a single sample reflector, is given by:

$$SNR_{SS-OCT} \approx M \frac{\rho R_S S_{TD-OCT}}{4 q_e B_{SS-OCT}} \tag{40}$$

where M is the number of samples, ρ is the detector's responsivity, R_S is the sample's reflectivity, S_{TD-OCT} is the sample's illumination power integrated over M, and B_{SS-OCT} is the noise equivalent bandwidth of the system. Since B_{SS-OCT}

depends on the frequency of the sweep, the SNR is affected by the properties of the used light source.

The selection of a laser source for SS-OCT is paramount and must consider several parameters such as wavelength sweep range, sweep repetition rate, the linearity of the sweep, radiant power, and instantaneous linewidth. [21]

As mentioned in the previous chapter, the wavelength range and the radiant power of a source depend on the studied sample and its characteristics. For instance, if imaging at a center wavelength of 1300 nm is desired, the wavelength range should be higher than 100 nm. This way the system operates in a region where the attenuation of biological tissues is low, and the resolution is equivalent to that of TD-OCT. On the other hand, these wavelengths are not suitable for eye imaging because of water absorption. [3][21] Also, the source's power should be high enough to preserve clinically relevant sensitivity, while not damaging the tissues. The sweep repetition rate of the source determines the A-scan acquisition frequency and the instantaneous linewidth determines the ranging depth and the sensitivity fall-off with depth. The linearity of the sweep is significantly related to the need of a highly linear k-space scan. In most SS-OCT implementations the interferograms are sampled with a non-uniform k interval that can lead to a degradation of axial resolution and ranging depth. Because of this, the non-linear data must be converted to linear-in-k data before the FT is applied. This calibration process can be achieved by implementing numerical algorithms or hardware solutions. For example, it is possible to sample the detector with non-uniform time intervals in order to produce uniform k-space sampling; another option is to re-sample the acquired data by interpolation to a uniform spacing in k. [21][26][27] Xi et. al [22] describe a method for real-time uniform k-space sampling using nonlinear-in-k calibration signal from a Mach-Zender interferometer.

One of the most convenient sources for SS-OCT that meets the necessary criteria are Fourier-domain mode-locked lasers (FDML), combining good imaging speed, instantaneous coherence length, and adequate spectral width. [22] This type of laser leads to an increase in imaging speed and depths.

FDML lasers are based on a fibre-ring geometry with a semiconductor optical amplifier (SOA) as a gain medium, and a fibre Fabry-Perot filter as the tunable, narrowband optical bandpass filter. In FDML, a dispersion managed line is incorporated into the laser cavity and the narrowband filter is tuned periodically at the cavity roundtrip time, producing a quasi-stationary operation mode. Light from one frequency sweep propagates through the laser cavity and returns to the filter at the exact time when the transmission window of the optical bandpass filter is tuned to the same optical frequency. Consequently, light from the previous round trip is coupled back to the gain medium. [28]

Figures 3.1 and 3.2 show a schematic of the FDML concept and a diagram of a high-speed, frequency swept FDML laser, respectively.

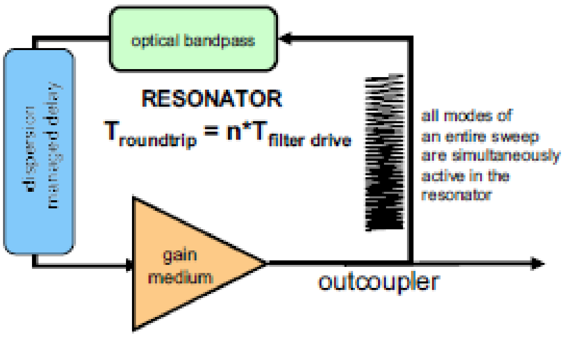
optical bandpass
RESONATOR
$T_{roundtrip} = n^*T_{filter\ drive}$
dispersion managed delay
all modes of an entire sweep are simultaneously active in the resonator
gain medium
outcoupler

Figure 3.1 Scheme of the FMDL concept. Reproduced from [28].

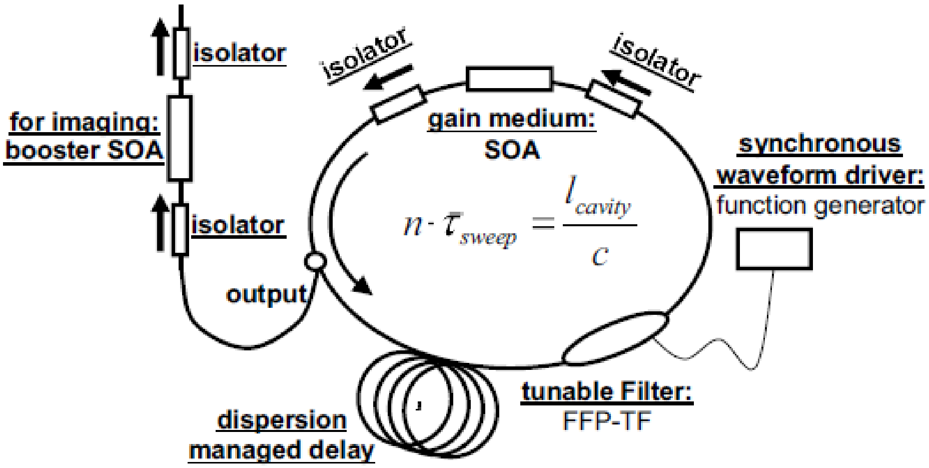
isolator
isolator
isolator
for imaging: booster SOA
gain medium: SOA
synchronous waveform driver: function generator
isolator
$n \cdot \tau_{sweep} = \frac{l_{cavity}}{c}$
output
dispersion managed delay
tunable Filter: FFP-TF

Figure 3.2 Diagram of an FDML high-speed, frequency swept laser. Reproduced from [28].

SS-OCT imaging over a 7 mm depth range, achieving sensitivities of around 108 dB, axial resolution of approximately 9 µm in tissue, and with a sensitivity roll off of 7.5 dB over 7mm was reported by Huber *et al*. [28]

3.2 SIMULATION OF THE SS-OCT SYSTEM

This section follows the mathematical treatment of an OCT system presented by Hee [29], and by Dhalla [30].

A simple Michelson interferometer is considered and the sample is replaced by a perfect mirror. The light source is assumed perfectly coherent and, therefore, the electric field components produced by the reference and sample mirrors, after reflection and recombination, are described as:

$$E_r = A_r exp[-j(2\beta_r l_r - \omega t)] \tag{41}$$

$$E_s = A_s exp[-j(2\beta_s l_s - \omega t)] \tag{42}$$

A_r and A_s are the field amplitudes, l_r and l_s are the reference and sample mirror positions, β_r and β_s are the propagation constants, and ω is the source's optical frequency. In free space, the propagations constants are equal and given by:

$$\beta_r = \beta_s = \frac{2\pi}{\lambda} \tag{43}$$

The photocurrent at the square-law detector is given by:

$$I = \langle \frac{\eta e}{h\nu} \left(\frac{|E_r + E_s|^2}{2\eta_0} \right) \rangle \tag{44}$$

where η is the detector's responsivity, e is the charge of the electron, $h\nu$ is the photon energy, and η_0 is the intrinsic impedance of free space.

Making the appropriate substitutions yields:

$$I = \frac{\eta e}{2h\nu\eta_0}\left(|A_r|^2 + |A_s|^2 + 2A_rA_s\,cos\left(2\pi\frac{\Delta l}{\lambda/_2}\right)\right) \tag{45}$$

with Δl being the difference between the reference and path lengths.

The last term in the previous equation represents the interference between the reference and sample fields and is described by a sinusoidal varying term.

Considering now a broadband source, the reference and sample fields become a function of optical frequency:

$$E_r(\omega) = A_r(\omega)exp[-j(2\beta_r(\omega)l_r - \omega t)] \tag{46}$$

$$E_s(\omega) = A_s(\omega)exp[-j(2\beta_s(\omega)l_s - \omega t)] \tag{47}$$

The interferometric photocurrent is proportional to the sum of the interference due to each monochromatic component of the light, and, therefore, is written as:

$$I \propto \Re\left\{\int_{-\infty}^{+\infty} S(\omega)exp[-j\Delta\phi(\omega)]\frac{d\omega}{2\pi}\right\} \tag{48}$$

where $\Re$ stands for the real component, $S(\omega)$ is equivalent to the light source's power spectrum, and $\Delta\phi(\omega)$ characterizes the phase mismatch at the detector for each frequency component:

$$\Delta\phi(\omega) = 2\beta_s(\omega)l_s - 2\beta_r(\omega)l_r \tag{49}$$

If the propagation constants are the same in each arm, β can be rewritten as a first-order Taylor expansion around the center frequency ω_0:

$$\beta(\omega) = \beta(\omega_0) + \beta'(\omega_0)(\omega - \omega_0) \tag{50}$$

The phase mismatch term is consequently given by:

$$\Delta\phi(\omega) = \beta(\omega_0)(2\Delta l) + \beta'(\omega_0)(\omega - \omega_0)(2\Delta l) \tag{51}$$

Substituting the last equation into equation (49), results in the detector photocurrent in a TD-OCT system:

$$I \propto \Re\left\{exp\left[-j\omega_0\Delta\tau_p\right]\int_{-\infty}^{+\infty} S(\omega - \omega_0)exp\left[-j(\omega - \omega_0)\Delta\tau_g\right]\frac{d(\omega-\omega_0)}{2\pi}\right\} \tag{52}$$

where $\Delta\tau_p$ and $\Delta\tau_g$ are the phase and group delay differences between the sample and reference, given by:

$$\Delta\tau_p = \frac{\beta(\omega_0)}{\omega_0}2\Delta l = \frac{2\Delta l}{v_p} \tag{53}$$

$$\Delta\tau_g = \beta'(\omega_0)2\Delta l = \frac{2\Delta l}{v_g} \tag{54}$$

In a swept source OCT system, each spectral channel centered at an instantaneous central frequency ω_c and with a finite linewidth function $\Delta\nu(\omega - \omega_c)$, is considered as a separate, single-depth TD-OCT measurement. So, the previous equations must be rewritten for an appropriate description of the system. All terms written in terms of ω_0 appear written as a function of ω_c, the source term becomes $S(\omega_c - \omega_0)\Delta\nu(\omega - \omega_c)$, and the phase and group delays also become a function of ω_c and are evaluated for each spectral channel.

Taking into account the aforementioned changes, the interferometric photocurrent is rewritten as:

$$I(\omega_c) \propto \Re\left\{S(\omega_c - \omega_0)\, exp\left[-j\omega_c \Delta\tau_p(\omega_c)\right] \times \int_{-\infty}^{+\infty} \Delta\nu(\omega - \omega_c) exp[-j(\omega - \omega_c)\Delta\tau_g(\omega_c)]\, \frac{d(\omega - \omega_c)}{2\pi}\right\} \tag{55}$$

It is assumed that the linewidth function has a Gaussian profile, normalized to integrate to unity, and with a standard deviation of $2\sigma_w$:

$$\Delta\nu(\omega - \omega_c) = \left(\frac{2\pi}{\sigma_w^2}\right)^{\frac{1}{2}} exp\left[\frac{(\omega - \omega_c)^2}{2\sigma_w^2}\right] \tag{56}$$

The SS-OCT photocurrent becomes:

$$I(\omega_c) \propto \Re\left\{S(\omega_c - \omega_0)exp[-j\omega_c \Delta\tau_p(\omega_c)]exp\left[-\frac{\Delta\tau_g^2(\omega_c)}{2\sigma_t^2}\right]\right\} \tag{57}$$

where the standard deviation $2\sigma_t$ is related to the standard deviation of the linewidth profile $2\sigma_w$:

$$2\sigma_t^2 = \frac{2}{\sigma_w^2} \tag{58}$$

Here σ_t is the characteristic width of the fall-off function. σ_w can be defined as:

$$\sigma_w = \frac{\Delta\omega}{2} = \frac{\omega_{i+1} - \omega_i}{2} \tag{59}$$

The material is considered to be non-dispersive, so the phase and group delays are equal and independent of frequency. Furthermore, it is assumed that $v_p = v_g = c$ and therefore:

$$\Delta\tau = \frac{2\Delta l}{c} \tag{60}$$

Equation (57) is rewritten as:

$$I(\omega_c) \propto \Re\left\{S(\omega_c - \omega_0)exp\left[-j\omega_c\left(\frac{2\Delta l}{c}\right)\right]exp\left[-\frac{\left(\frac{2\Delta l}{c}\right)^2}{2\sigma_t^2}\right]\right\} \tag{61}$$

The first exponential term represents the phase mismatch and the second represents the signal fall-off due to a loss of fringe visibility.

The A-scans are obtained by applying the Fourier transform over $\omega_c - \omega_0$:

$$i(t) \propto \left[s(t) * \frac{1}{2}\big(\delta(t-\Delta\tau)+\delta(t+\Delta\tau)\big)\right] \times exp\left[-\frac{\Delta\tau^2}{2\sigma_t^2}\right] cos(-\omega_0\Delta\tau) \qquad (62)$$

$s(t)$ is the FT of the source spectrum and represents the axial resolution, which is convolved with a pair of delta functions that represent the positive and negative positions of a sample reflector. The exponential term on equation (61) remains the same, because it only depends on the function of delay $\Delta\tau$. Due to the evaluation of the FT about ω_0, the cosine term is introduced on the equation and it represents a rapid modulation in depth. This term is equivalent to the carrier frequency in TD-OCT and, in practice, it is not detected, since its frequency is too high when compared with the inverse of the detector’s time constant.

Now, an analysis of Group Velocity Dispersion (GVD) is included in the equations. GVD prompts a propagation of light with nonlinearly frequency-dependent phase delays. When there is significant GVD mismatch between the arms of the interferometer, the axial PSF, i.e. the interferometric autocorrelation, broadens leading to deterioration of the OCT system’s axial resolution.

Considering GVD the Taylor expansion of the propagation constant becomes:

$$\beta(\omega) = \beta(\omega_0) + \beta'(\omega_0)(\omega - \omega_0) + \frac{1}{2!}\Delta\beta''(\omega_0)(\omega - \omega_0)^2 \tag{63}$$

and the phase mismatch term is rewritten as:

$$\Delta\phi(\omega) = \beta(\omega_0)(2\Delta l) + \beta'(\omega_0)(\omega - \omega_0)(2\Delta l) + \frac{1}{2}\Delta\beta''(\omega_0)(\omega - \omega_0)^2(2L) \tag{64}$$

$\Delta\beta''$ is the GVD mismatch between the sample and the reference paths over a mismatch length defined by $2L$.

If the three mentioned terms (phase mismatch, signal fall-off, and GVD mismatch) are combined, the interferometric photocurrent for a TD-OCT system is given by:

$$I \propto \Re\left\{exp[-j\omega_0\Delta\tau_p]\int_{-\infty}^{+\infty} S(\omega - \omega_0)\, exp[-j(\omega - \omega_0)\Delta\tau_g] exp[-j\frac{1}{2}\Delta\beta''(\omega_0)(\omega - \omega_0)^2(2L)]\,\frac{d(\omega - \omega_0)}{2\pi}\right\} \tag{65}$$

For an SS-OCT system, the signal represented by equation (61) is rewritten as:

$$I(\omega_c) \propto \Re\left\{S(\omega_c - \omega_0)\, exp\left[-j\omega_c\Delta\tau_p\right] exp\left[-\frac{\Delta\tau_g^2}{2\sigma_t^2}\right] exp\left[-j\frac{1}{2}\Delta\beta''(\omega_c - \omega_0)^2 \times (2L)\right]\right\} \tag{66}$$

The GVD mismatch can be minimized by careful construction of the OCT system. In fibre-based systems, the length of fibre should be equal in the reference and sample arms and the dispersion on the sample tissues should be compensated on the reference arm (e.g. using a water cuvette). As it is possible to make $\Delta\beta'' \approx 0$, the exponential term containing the GVD mismatch is approximately 1. Consequently, this term can be neglected.

3.2.1 Conversion from Optical Frequencies to Electrical Frequencies

The previous equations are written in terms of the source's optical frequency ω. However, it is useful to describe the SS-OCT system using functions depending on the electrical frequency $\widetilde{\omega}$.

Following [29] it is possible to define a correspondence between the source's power spectrum in the optical frequency domain and the interferometric photocurrent in the electrical frequency domain. To accomplish this, a linear transformation $T(\omega)$ between optical frequencies and electrical frequencies is established:

$$\widetilde{\omega} = T(\omega) = \frac{2v_s}{v_g}\left[\omega - \omega_0\left(\frac{v_g}{v_p} - 1\right)\right] \tag{67}$$

In a TD-OCT system, v_s is defined as the velocity of the reference mirror while oscillating during scanning. For an SS-OCT system, it is considered that v_s is the velocity of the source's sweep during one acquisition.

Considering that both the phase velocity (v_p) and the group velocity (v_g) are equal to the speed of light in vacuum (c), the previous equation can be simplified and becomes:

$$\widetilde{\omega} = T(\omega) = \frac{2v_s}{c}\omega \tag{68}$$

Following this conversion, the previously stated equations can be rewritten in terms of the electrical frequency $\widetilde{\omega}$. The phase mismatch term becomes proportional to:

$$exp\left[-j\frac{\Delta l}{v_s}\widetilde{\omega}\right] \tag{69}$$

the term related to the signal fall-off is rewritten as:

$$exp\left[-\Delta l^2\frac{(\widetilde{\omega}_{i+1} - \widetilde{\omega}_i)^2}{8v_s^2}\right] \tag{70}$$

and the GVD term becomes:

$$exp\left[-j\Delta\beta''\frac{c^2}{4v_s^2}\widetilde{\omega}^2 L\right] \tag{71}$$

3.3 SS-OCT SYSTEM LAYOUT

Figure 3.3 illustrates a simplified schematic of the swept-source OCT system layout that is being developed at IBILI. This system is made up by an OCT Swept Source Engine from Axsun, a balanced amplified photodetector from Thorlabs (PDB471C), and several fibre optic couplers with different splitting ratios also from Thorlabs (FC1064-50B-APC and FC1064-90B-APC).

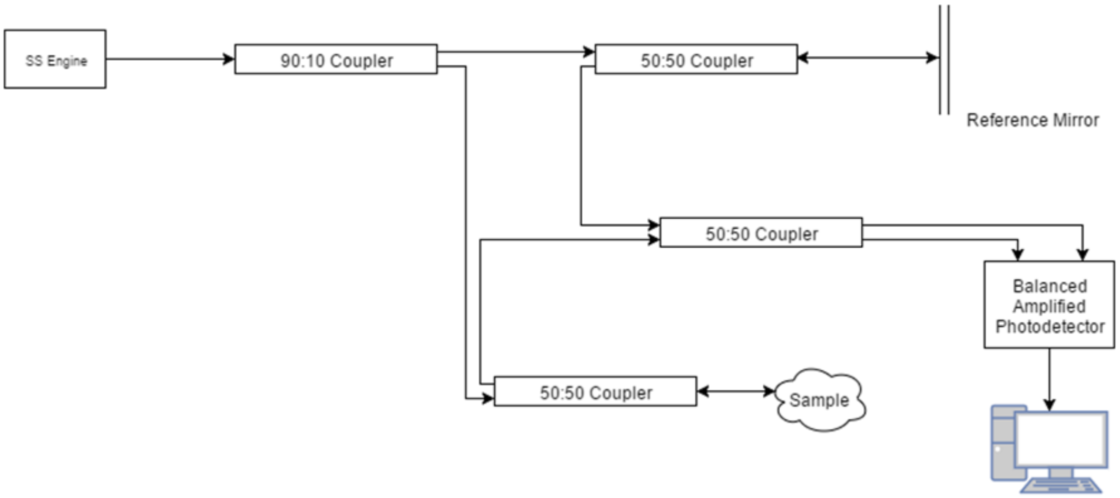
SS Engine
90:10 Coupler
50:50 Coupler
Reference Mirror
50:50 Coupler
Balanced Amplified Photodetector
50:50 Coupler
Sample

Figure 3.3 Simplified scheme of the layout of the SS-OCT system.

The light beam emitted by the source is split by a 90:10 optic coupler. 90% of the incident light is sent into the sample path, and the remaining light is coupled into the reference path. At the reference path, the light passes through a 50:50 optic coupler and is reflected by a mirror. The light at the sample path also passes through a 50:50 optic coupler and is reflected by the different structures within the studied object. The reference and sample light beams are recombined at a final 50:50 optic coupler. Finally, the resulting beam is split in order to be detected by the balanced detector. The obtained signal is digitally converted and processed by a computer.

3.3.1 Axsun Swept Source Engine

The system in development uses a swept source laser engine from Axsun Technologies (Billerica, Massachusetts, USA), with a specified center wavelength of $1060\ nm$ and wavelengths ranging from $980\ nm$ to $1100\ nm$. The Axsun SS Engine features high sweep speed and optical power, and a broad tuning bandwidth. This engine has a minimum average output power of $15\ mW$, operates at a fixed sweep rate within a range of $10 - 100\ kHz$, has a minimum coherence length of $10\ mm$, and a $10\ dB$ fall-off within the specified wavelength range. [31]

In the table below the typical operating and scanning parameters of the SSOCT-1060 engine are listed.

Table 1. Operating and scanning parameters of the SSOCT-1060 engine.

Parameter	Value
Wavelength Range	$985.0 - 1095.0\ nm$
Scan Range in Air	$3.7\ mm$
Sweep Frequency	$100\ kHz$
Maximum Samples	1510
Selected Number of Samples	1376
Percent Bandwidth Used	91%
Duty Cycle	45%
Estimated Clock Frequency[1]	$310\ MHz$

1 ±20% Typical Variation

The following figure shows the time-averaged spectral power output of a typical SSOCT-1060 engine.

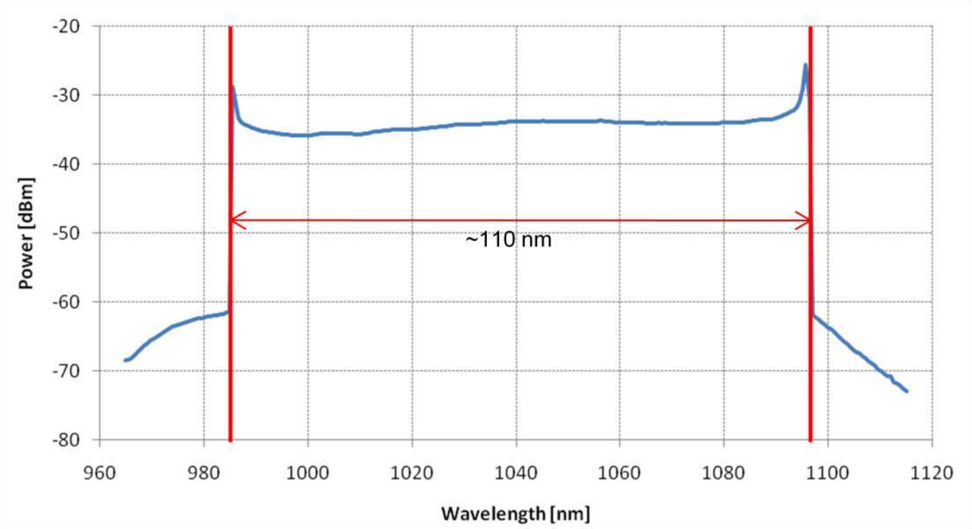

Figure 3.4 Time-averaged spectral power output of the SSOCT-1060 engine. Reproduced from [31].

In the figure below the trigger and optical power of the engine are graphically represented.

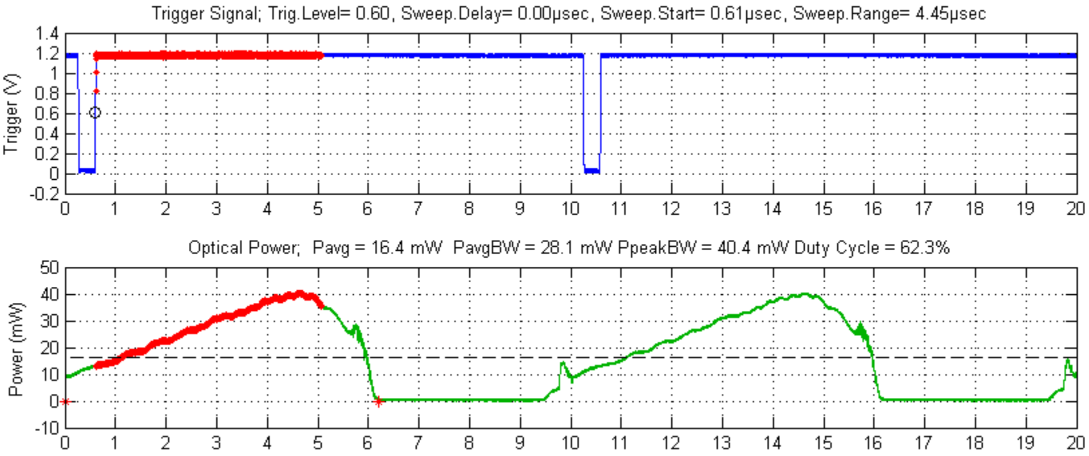

Figure 3.5 Trigger signal and optical power of the SSOCT-1060 engine as a function of time (µs). Reproduced from [31].

The frequency range of the source is entirely swept during the tuning process, which consists of an ascending phase and a descending phase. The ascending phase corresponds to the duty cycle, and lasts around 4.5 µs. During this phase the laser is turned on and the frequency range is swept. During the descending phase, the laser is turned off and the source's filter returns to the original state.

3.3.2 Thorlabs Balanced Amplified Detector – PDB471C

The signal detection on the OCT system is accomplished by the use of a Thorlabs (Newton, New Jersey, USA) PDB471C balanced amplified detector. This detector consists of two matched pigtailed InGaAs photodiodes, and an ultra-low distortion and high-speed trans-impedance amplifier, as shown in figure 3.6. The detector also has two monitor outputs that allow the user to check the optical input power level on each photodiode, separately. [32]

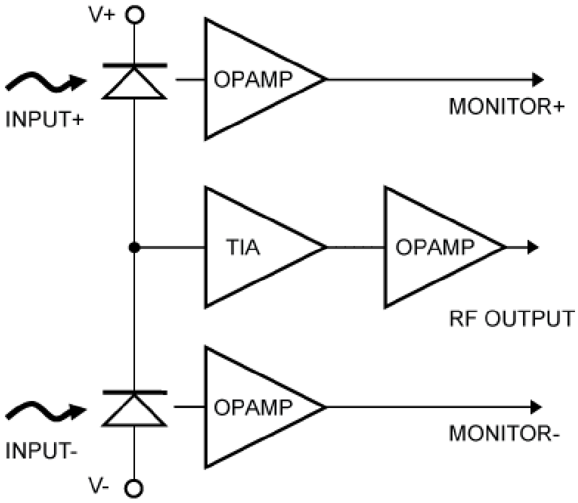

Figure 3.6 Schematic of the balanced amplified detector. Reproduced from [32].

The produced output voltage ($U_{RF,OUT}$) is proportional to the difference between the photocurrents of each photodiode (i.e. the difference between the two optical input signals $P_{Opt,1}$ and $P_{Opt,2}$).

$$U_{RF,OUT} = \left(P_{Opt,1} - P_{Opt,2}\right) \times R(\lambda) \times G \tag{72}$$

$R(\lambda)$ is the responsivity of the photodiode at a given wavelength, and G is the transimpedance gain. The responsivity is defined at 1060 nm as 0.72 A/W, and for other wavelengths, can be determined by the graph represented on the following figure.

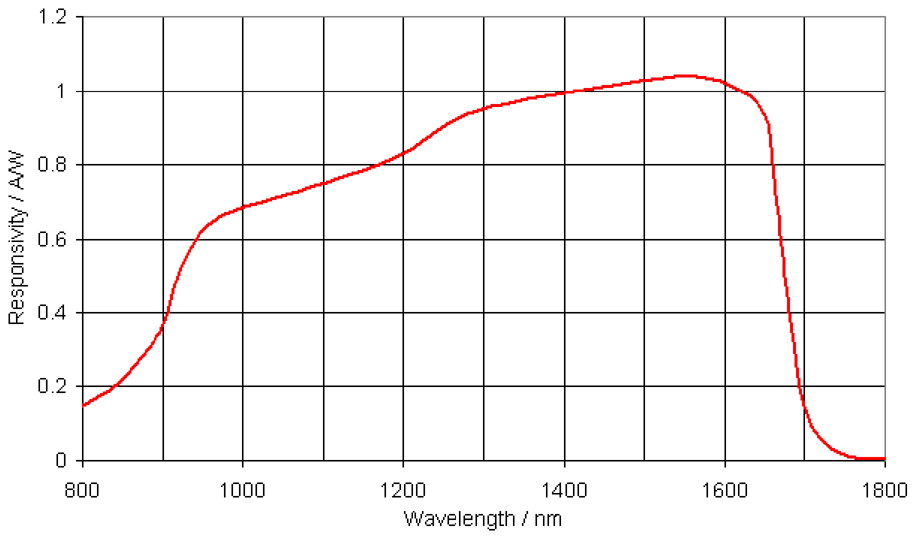

Figure 3.7 Responsivity of the PDB471C balanced photodetector as a function of the wavelength of the incident radiation. Reproduced from [32].

As shown in the previous figure, the detector is responsive to radiation with wavelengths ranging from 900 nm to 1600 nm. Furthermore, its bandwidth, which limits the maximum detectable depth, is defined as 400 MHz, meaning that frequencies over this value will be attenuated. The frequency response of the detector is represented on figure 3.8.

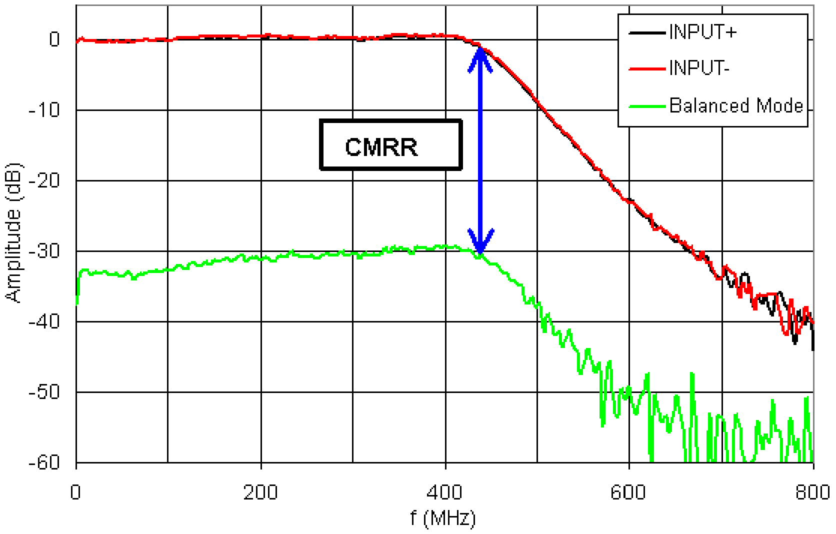

Figure 3.8 Frequency response of the Thorlabs PDB471C balanced amplified photodetector. Reproduced from [32].

The frequency of the OCT signal is proportional to the frequency of the source's sweep (f_{sweep}), the sweep interval (Δk), and the path length difference. The maximum signal frequency can be determined as:

$$f_{max} = \Delta k \times f_{sweep} \times \frac{z_{max}}{\pi} \tag{73}$$

The sweep interval is determined as $\Delta k = 2\pi \left(\frac{1}{989nm} - \frac{1}{1090nm}\right) \cong 5.9 \times 10^5\ m^{-1}$ (the light source's operating wavelengths range from 989 nm to 1090 nm) and the source's effective sweep frequency is 200 kHz. The maximum depth (z_{max}) is determined by equation (18) and, for the mentioned operating wavelength range with 1376 sampling points, it has a value of 3.51 mm. Therefore, the OCT signal has a maximum frequency of $\sim 132\ MHz$. Since the photodetector's bandwidth is larger than the maximum frequency of the generated signal, the maximum depth sensitivity of the system will not be limited by the detector.

The CMRR, Common Mode Rejection Ratio, represented on figure 3.8, measures the rejection of unwanted input signals common to both optical inputs, relative to the desired differential signal. The CMRR specifies how much of the common mode signal will appear in the final measurement. Ideally, the CMRR should be infinite. In practice, it must be high enough so that the excess photon noise is suppressed, leading to an increased SNR.

The following table summarizes the main characteristics of the balanced detector.

Table 2. Main characteristics of the PDB471C Thorlabs Balanced Amplified Photodetector.

PDB471C Balanced Amplified Detector	
Detector Type	InGaAs/PIN
Operating Wavelength	$1060\ nm$
Coupling Loss	$< 1.0\ dB$ ($< 0.3dB$ Typ.)
Typical Max. Responsivity	$0.72\ A/W$ @ $1060\ nm$
Optical Back Reflection	$< -40\ dB$
RF Output	
Bandwidth (3dB)	DC – $400\ MHz$
CMMR	$> 25\ dB$ ($> 30\ dB$ Typ.)
Transimpedance Gain	$10 \times 10^3\ V/A$
Conversion Gain	$7.2 \times 10^3\ V/W$ @ $1060\ nm$
Impedance	$50\ \Omega$
Minimum NEP	$8\ pW/\sqrt{Hz}$ (DC to $100\ MHz$)
Overall Output Voltage Noise	$< 2.0\ mV_{RMS}$

3.3.3 Thorlabs Fibre Optic Couplers - FC1064-50B-APC and FC1064-90B-APC

The SS-OCT system described uses four bidirectional, single-mode 2x2 fused fibre couplers from Thorlabs. Three of them have a 50:50 coupling ratio (FC1064-50B-APC), and one has a 90:10 coupling ratio (FC1064-90B-APC). All the couplers have a specified center wavelength of $1064\,nm$. The coupler's fibres have a numeric aperture $NA = 0.22$. [33]

The coupler's insertion loss and excess loss are important specifications and can be determined by equations (74) and (75), respectively. The insertion loss is defined as the ratio of the input power (P_{In}) to the output power (P_{Out}) at one of the outputs of the coupler. The excess loss is defined as the ratio of the total output power ($P_{Port3} + P_{Port4}$) to the total input power (P_{Port1}).

$$Insertion\ Loss\ (dB) = 10\log\left(\frac{P_{In}(mW)}{P_{Out}(mW)}\right) \tag{74}$$

$$Excess\ Loss\ (dB) = -10\log\left(\frac{P_{Port3}(mW) + P_{Port4}(mW)}{P_{Port1}(mW)}\right) \tag{75}$$

The mentioned input and output ports are represented in figure 3.9.

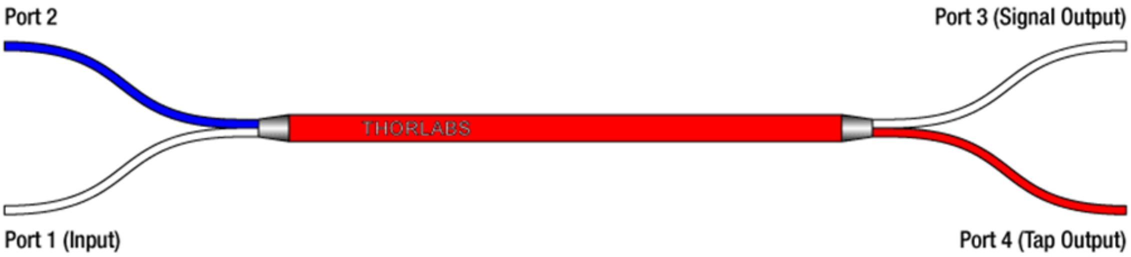

Figure 3.9 Graphical representation of the fibre optic coupler's ports. Reproduced from [33].

The directivity of the couplers, i.e. the fraction of input light that exits the coupler through an input port instead of the intended output port, is calculated using equation (76):

$$Directivity\ (dB) = 10\log\left(\frac{P_{Port1}(mW)}{P_{Port2}(mW)}\right) \tag{76}$$

The following table lists the main specifications of the used couplers.

Table 3. Listing of the main specifications of the fibre optic couplers.

Parameter	**FC1064-50B-APC**	**FC1064-90B-APC**
Coupling Ratio	50:50	90:10
Insertion Loss	$3.5\ dB$ / $3.5\ dB$	$0.7\ dB$ / $10.5\ dB$
Excess Loss	$0.12\ dB$	
Directivity	$> 55\ dB$	
Center Wavelength	$1064\ nm$	

4. SIMULATION METHODS AND RESULTS

The work carried out can be summarized in two main blocks: simulation of a simple OCT system, based on the configuration of a Michelson interferometer, and simulation of the swept-source OCT system developed at IBILI.

The main purpose of the SS-OCT simulation was to simulate two of the main OCT parameters, namely the sensitivity fall-off, and the axial resolution. The values of these two parameters, as well as the values of the system's sensitivity and dynamic range, are crucial to obtain good quality images in biomedical applications. Table 4 lists the minimum values for the aforementioned parameters.

Table 4: Minimum values for the main OCT parameters in biomedical applications.[34]

Parameter	Value
Axial Resolution	$< 10\ \mu m$
Sensitivity Fall-Off	$20\ dB$ over $2\ mm$ ranging depth
Dynamic Range	$40 - 50\ dB$
Sensitivity	$> 95 dB$

All the simulations were accomplished using MATLAB® and the source codes can be consulted in the final annexes.

4.1 TIME DOMAIN OCT SIMULATION

The first step of the work was to simulate a simple Time Domain OCT system, as described in section 1.1.

First, a Gaussian spectrum was defined using the *gaussmf* function. This function creates a Gaussian shaped curve of amplitude 1, with input parameters ω, σ and ω_c. ω is a vector containing the optical frequency values, σ is the standard deviation of the function, defined in terms of ω, according to equation (77), and ω_c is the desired center frequency.

$$\sigma = \frac{2\pi c \frac{\Delta\lambda}{\lambda_0^2}}{\sqrt{8\ln(2)}} \tag{77}$$

For the purpose of the simulation $\lambda_0 = 800\,nm$ and $\Delta\lambda = 50\,nm$. Taking into account the relation between the wavelength and the frequency, demonstrated by the following equation:

$$\omega = \frac{2\pi c}{\lambda} \tag{78}$$

the center frequency of the defined Gaussian spectrum is $\omega_c = 2.356 \times 10^{15}\,rad\,s^{-1}$. The vector ω was defined as a linearly spaced array of 1024 elements, ranging from $\omega_c - \frac{\omega_c}{3}$ to $\omega_c + \frac{\omega_c}{3}$. The simulated source spectrum is represented on figure 4.1.

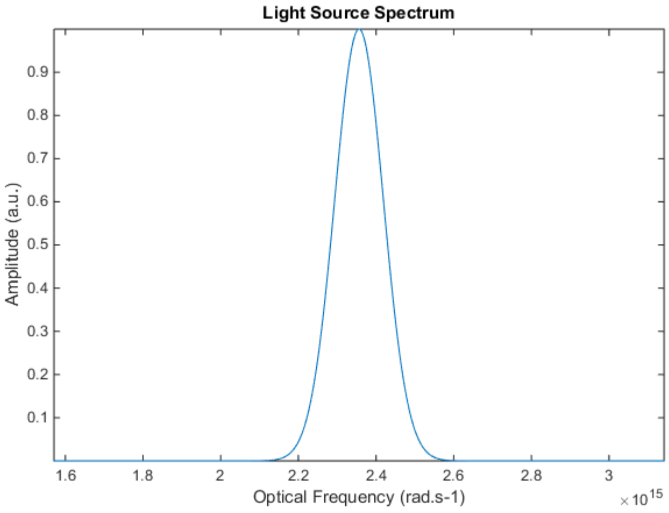

Figure 4.1 Simulated spectrum of a Gaussian light source with parameters $\lambda_0 = 800\ nm$ and $\Delta\lambda = 50\ nm$, defined as a function of the optical frequency.

Next, a function describing the sample ($H[\omega]$), was constructed following equations (79) and (80).

$$H[\omega] = \sum_{k=1}^{j-1} r_j exp\left[2i\frac{\omega}{c}n_k z_k\right] \tag{79}$$

$$r_j = \frac{n_{k+1} - n_k}{n_{k+1} + n_k} \tag{80}$$

where r_j is the reflectivity of each layer j of the sample, calculated from the refractive indices of adjacent layers n_k, and z_k is the thickness of each layer j. $H[\omega]$ is calculated for each value of the optical frequency (ω) array.

Considering a multi-layered object, both the refractive indices (n) and the thickness of the layers (z) were defined through arrays with the desired values. A theoretical three layered sample, with the characteristics listed on the table below, was considered.

Table 5. Characteristics of a theoretical sample with three layers, as described in [1].

Layer j	**Refractive index n**	**Layer Thickness z (μm)**
1	1.00	5.00
2	1.30	15.00
3	1.50	30.00
4	1.00	0.00

Following equations (81) and (82), the TD-OCT signal was calculated, resulting in a plot of amplitude *vs*. the reference mirror displacement. This plot represents the OCT interferogram.

$$\varphi[x] = cos\left[2 \cdot x \cdot \frac{\omega}{c}\right] \tag{81}$$

$$I_{TD} = \Re\left\{\frac{1}{2} \cdot S[\omega] \cdot H[\omega] \cdot \varphi[x]\right\} \tag{82}$$

where $\varphi[x]$ is the phase mismatch caused by the mirror displacement, which is represented by x, a linearly spaced array ranging from 0 to 100 µm. I_{TD} is the TD-OCT signal, which depends on the Gaussian spectrum $S[\omega]$ shown in figure 4.1, on the sample's function $H[\omega]$, and on the phase mismatch $\varphi[x]$.

For the represented source and considering the defined sample, it was expected to obtain a graphical representation of an OCT interferogram where three amplitude peaks could be identified. Since the thickness of the layers can be determined as the quotient of the distance between the peaks and the respective refractive indices, the location of the peaks can be easily inferred. On air, the first one should appear at approximately 5 µm from the origin ($x = 0$), the second at *circa* 25 µm, and the last at around 70 µm.

Figure 4.2 shows the resulting interferogram.

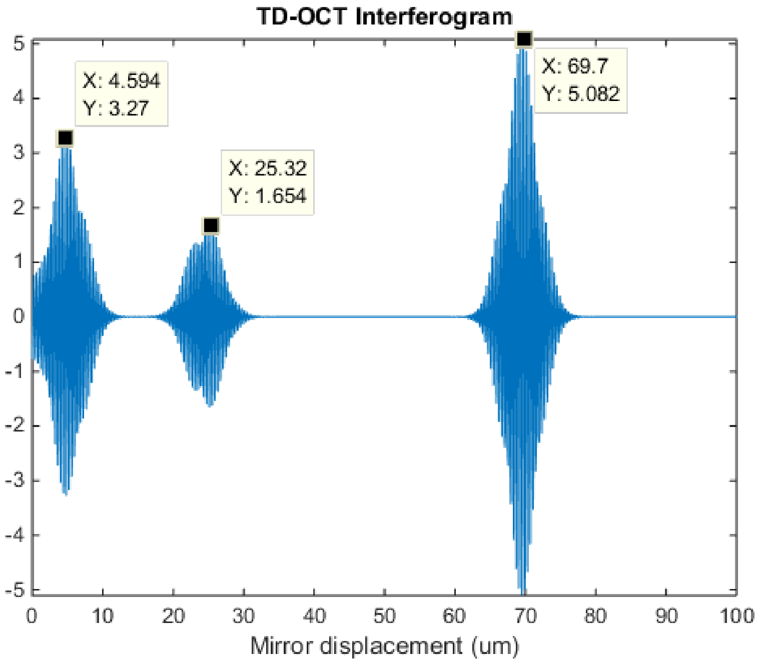

Figure 4.2 Obtained interferogram for the Time Domain OCT simulation. Three different peaks, corresponding to the sample's layers, can be identified: the first located at $x = 4.594\ \mu m$, the second located at $x = 25.32\ \mu m$, and the last located at $x = 69.7\ \mu m$.

4.2 FOURIER DOMAIN OCT SIMULATION

The FD-OCT simulation was also based on a simple OCT detection scheme, as the previous simulation.

For the purpose of this simulation, the source spectrum $S[\omega]$ and the theoretical sample described on 4.1, defined by the function $H[\omega]$, were considered again. The OCT signal was calculated through equation (83), leading to the graph of amplitude *vs.* optical frequency represented on the figure 4.3.

$$I_{FD} = \frac{1}{4}S[\omega]|H[\omega]|^2 + \frac{1}{4}S[\omega] + \frac{1}{2}\Re\{S[\omega]H[\omega]\} \tag{83}$$

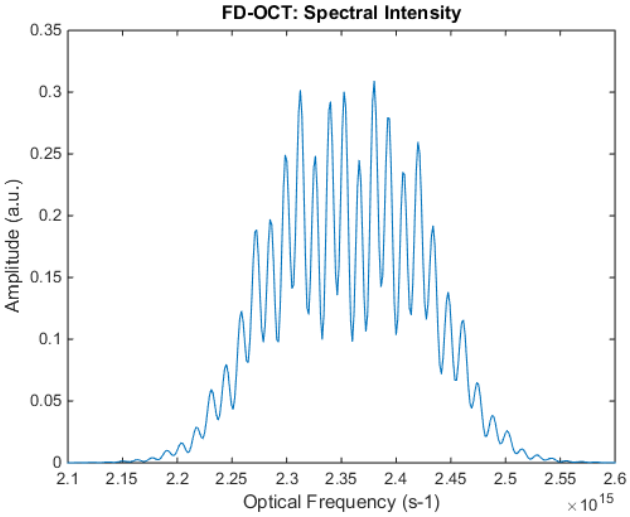

Figure 4.3 Detected spectral intensity of a Fourier Domain OCT detection scheme.

To conclude the simulation, a discrete Fourier transform (DFT) algorithm was computed, using the *ifft* function. This function returns the inverse DFT of the input vector, i.e. the OCT signal I_{FD}. The result of the *ifft* implementation was a graphical representation of an OCT A-scan, shown in figure 4.4.

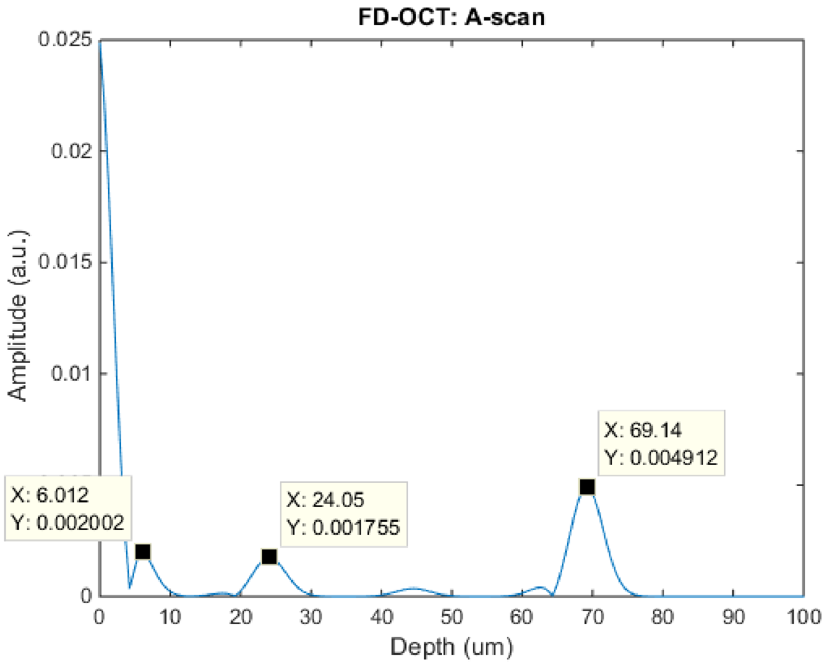

Figure 4.4 A-scan of the theoretical sample defined in 4.1, for an FD-OCT detection scheme. At $x = 0$, the so-called dc component of the FT is evident. The three peaks corresponding to the sample's three layers can be identified: the first located at $x = 6.012\ \mu m$, the second located at $x = 24.05\ \mu m$, and the last located at $x = 69.14\ \mu m$. Three small peaks relative to the self-interference component of equation (8) can also be distinguished.

The FD-OCT simulation results are in line with the obtained results for the TD-OCT simulation, regardless of some minor deviations of the position of the peaks.

4.3 SWEPT-SOURCE OCT SIMULATION

The simulation of the SS-OCT system was based on the system developed at IBILI. A simplified version of the detection scheme is graphically represented in section 3.3.

For the purpose of this simulation, we considered the power spectrum of the Axsun Swept Source Engine, using wavelengths ranging from 989 nm to 1090 nm. In order to simulate the spectrum, its graph was digitized using *Plot Digitizer*, a free software used to digitize scanned plots of functional data. However, due to the need of a linearly spaced array, as mentioned in 3.1, it was necessary to implement an interpolation algorithm. This was made using the *interp1* function with input parameters ω, P and ω'. ω is an array with the digitized optical frequency values and P is an array with the corresponding digitized power values. ω' is the new linearly spaced array of optical frequencies, ranging from $\frac{2\pi c}{1090nm}$ to $\frac{2\pi c}{989nm}$. The *pchip* interpolation (i.e. Shape-preserving piecewise cubic interpolation) method was used. In figure 4.5 both the digitized graph and the result from the interpolation are shown. The simulated power array represents the light beam that is emitted by the source.

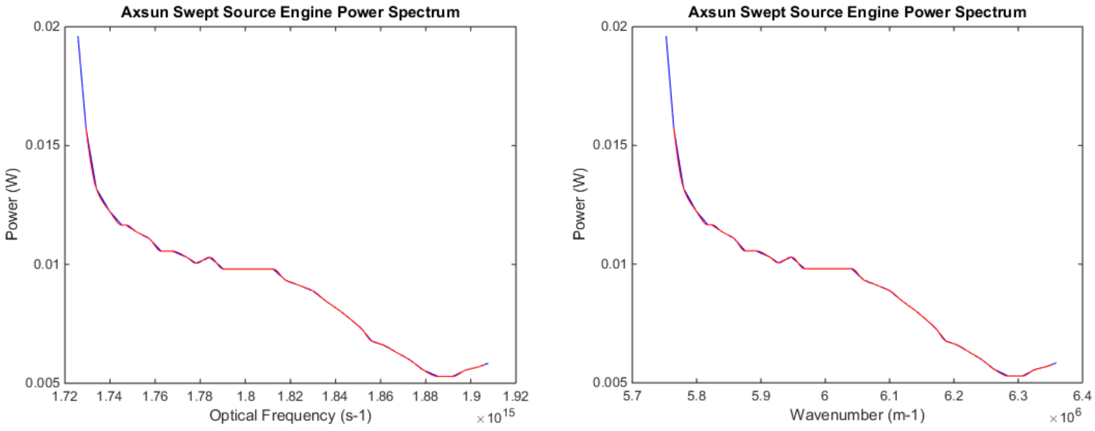

Figure 4.5: Power spectrum of the Axsun Swept Source Engine. The blue line represents the digitized values, and the red line represents the result of the interpolation. The graph on the left is the representation of the source's power as a function of the optical frequency ω, and the graph on the right is the representation of the source's power as a function of wavenumber k.

To simulate the coupling of the light beam into the first coupler, the power array was multiplied by the coupling ratio of the coupler, following equations (84) and (85):

$$A_{Ref}(W) = \sqrt{0.099 \times S[\omega]} \tag{84}$$

$$A_{Sample}(W) = \sqrt{0.901 \times S[\omega]} \tag{85}$$

A_{Ref} and A_{Sample} are the arrays that represent the amplitude of the light coupled into the reference and sample paths, respectively.

The light at the reference path is coupled into a 50:50 array and is reflected by a mirror with reflectivity r. The equation describing the amplitude of the final reference beam is:

$$A'_{Ref} = \sqrt{0.536 \times 0.479} \times A_{Ref} \times r \times P_{l\_r} \tag{86}$$

where P_{l_r} is a constant that accounts for the power losses at the couplers in the reference path.

In the sample path, the light beam is coupled into another 50:50 coupler, and it will interfere with the studied sample, described by the function written in equation (79).

The amplitude of the final sample beam is described by the following equation:

$$A'_{Sample} = \sqrt{0.536 \times 0.479} \times A_{Sample} \times P_{l\_s} \tag{87}$$

where P_{l_s} is a constant accounting the power losses at the couplers in the sample path.

The interference beam results from the recombination at a 50:50 coupler. The amplitude of the recombined beam is given by equation (88).

$$A_{rec} = A'_{Ref} + A'_{Sample} \tag{88}$$

Because we are using balanced detection, the final beam is split at the 50:50 coupler. The splitting of the recombined beam is described by the following equations:

$$A_1 = \sqrt{0.536}\, A_{rec} \times P_{l\_1} \tag{89}$$

$$A_2 = \sqrt{0.479}\, A_{rec} \times P_{l\_2} \tag{90}$$

Again, P_{l_1} and P_{l_2} are constants that account for the power that is lost at the last

50:50 coupler.

At each optical input of the photodetector, the photocurrent is calculated as:

$$i_{ph1} = R \times real[A_1 \times \varphi_{\Delta l} \times \tau \times H[\omega]] \tag{91}$$

$$i_{ph2} = R \times real[A_2 \times \varphi_{\Delta l} \times \tau \times H[\omega]] \tag{92}$$

where $\varphi_{\Delta l}$ and τ are the phase mismatch and signal fall-off terms, respectively. These terms were previously described by equations (69) and (70). R is the responsivity of the photodetector and $H[\omega]$ is the function that describes the studied sample. However, if we make an analysis of parameters like the sensitivity fall-off and the axial resolution, $H[\omega]$ is replaced by the reflectivity of a perfect mirror.

It should be noted that the GVD term was neglected, since, as explained in section 3.2.1, its value was considered to be approximately 1.

Following the schematic of figure 3.6, the voltage output of the balanced detector is simulated as:

$$V_{Out} = \left(i_{ph1} - i_{ph2}\right) \times G \tag{93}$$

where i_{ph1} and i_{ph2} are the currents generated in each input, and G is the detector's transimpedance gain.

The photodetector's noise was simulated taking into account the Noise Equivalent Power (NEP), whose value is mentioned in table 2. The NEP is defined as the radiant power that results in a signal equal to the observed noise, i.e. that results in an SNR equal to one. Usually, it is normalized to a unit bandwidth, with units of $W/\sqrt{Hz}$. In order to create a noise signal array, the function *wgn* was used. This function generates a matrix of white Gaussian noise, with a specified power, and a default load impedance of 1Ω. Equation (94) describes the detector's output with the added noise.

$$V = V_{Out} + NEP \tag{94}$$

Furthermore, a Butterworth low-pass filter with cutoff frequency of 400 MHz was created using MATLAB's *fdatool*. This filter simulates the detector's frequency response. Using the *filter* function, the created filter was applied to the voltage output array V, thus creating the final OCT interference signal. Figure 4.6 shows the magnitude response of the simulated filter.

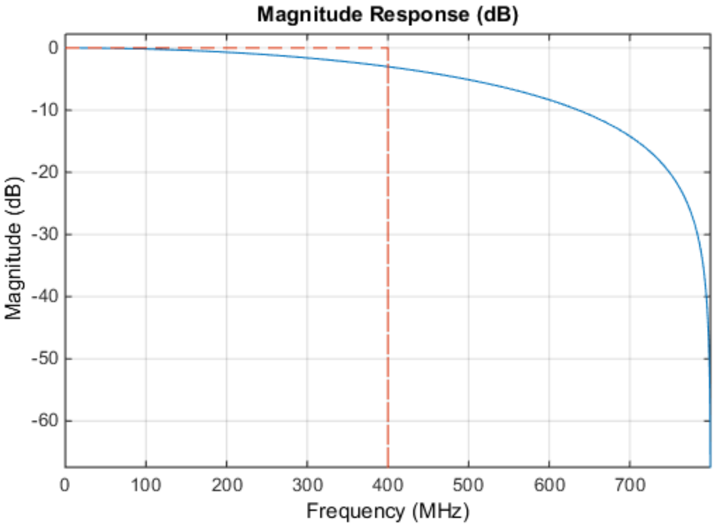

Figure 4.6 Magnitude response of the filter simulating the frequency response of the balanced detector.

Finally, the Fourier Transform of the signal was computed, using the *ifft* function, and half of the transform was graphically represented, as a function of depth. The obtained graph represents the A-scan of the studied sample.

The described method was used to simulate two fundamental OCT parameters: the sensitivity fall-off, and the axial resolution. A-scans of the theoretical sample described in section 4.1, and of a glass cover slip were also simulated.

4.3.1 Sensitivity Fall-off Simulation

In practice, the measurement of the sensitivity fall-off is accomplished by moving the reference mirror over a certain range so that the path length mismatch between the reference and sample arms varies. For each mirror position, the sensitivity of the PSF peak is determined according to equation (95):

$$S_{PSF}(dB) = 20\log(Amplitude_{PSF}) \tag{95}$$

For the purpose of the simulation, the array representing the reference beam was multiplied by the reflectivity of a perfect mirror, i.e. $r = 1$, and the simulation was performed for different values of the path length mismatch, ranging from 20 µm to 4 mm with 20 µm intervals. The following graph, representing the amplitude of the PSF for each mirror position as a function of the path length mismatch, was obtained.

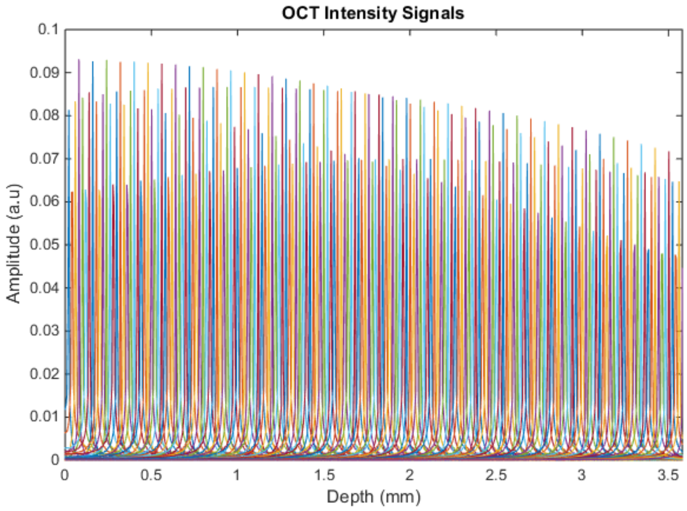

Figure 4.7 Graphical representation of the simulated OCT intensity signals.

To determine the sensitivity fall-off, the maximum amplitude of the peaks was represented on a logarithmic scale. The obtained graph is represented in the following figure.

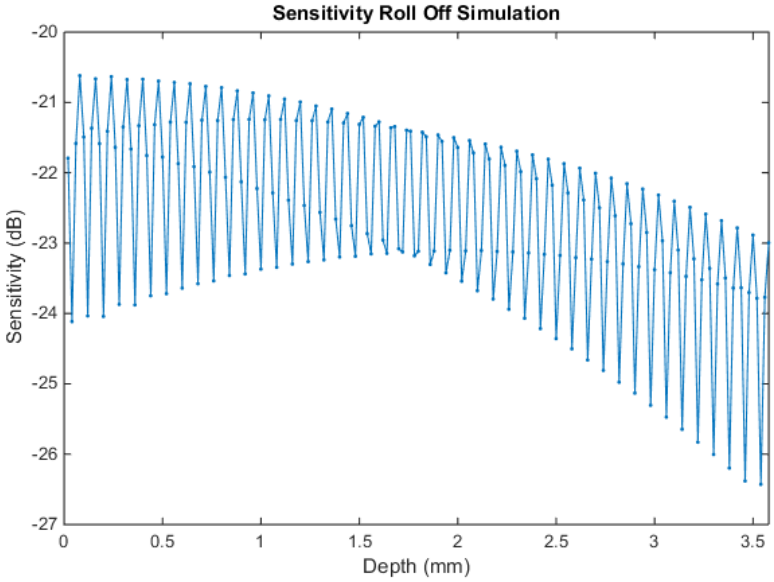

Figure 4.8: Sensitivity Fall-off Simulation. Graphical representation of peak sensitivity (dB) as a function of depth. An oscillation of the PSF peak values is visible.

Observing the previous graph, it is obvious the presence of an oscillation of the PSF peak values. This oscillation occurs with a period of 80 µm, i.e. every 80 µm the peak sensitivity returns to a maximum or minimum value, and it is due to the cosine term of the FT, described on equation (62). Experimentally this term is not detected.

To simulate accurately the sensitivity fall-off of the system, a peak sensitivity range from 20 µm to 3.58 mm, with 80 µm intervals was used. These values were represented as a function of depth and a linear regression was performed. In order to compare the simulated values to the experimentally obtained ones, two fits were made: one to the first 1.5 mm, and the other from 1.5 mm to 3.58 mm. The obtained graph is represented on figure 4.9.

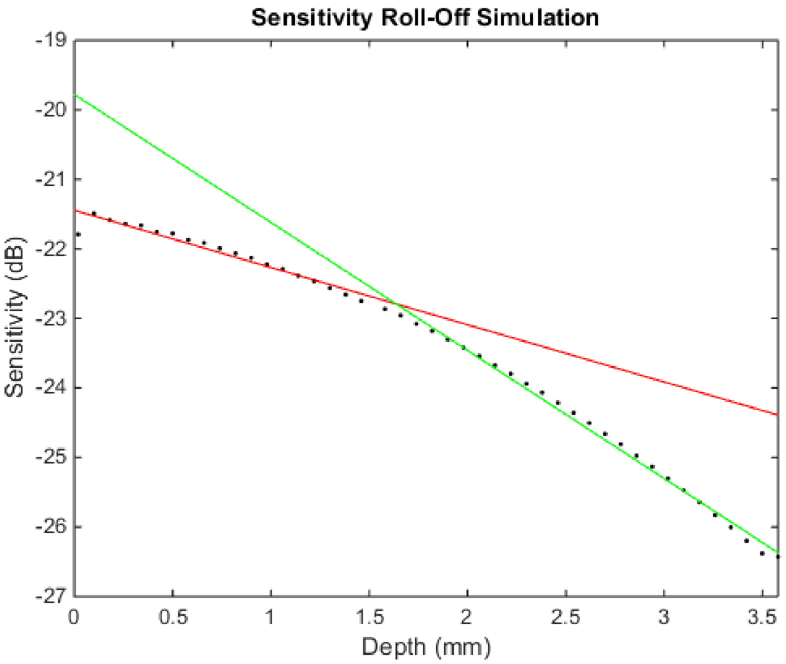

Figure 4.9 Sensitivity Fall-off Simulation. Peak sensitivity as a function of depth and graphical representation of the linear regression. The linear fit made to the first dataset, ranging from 20µm to 1.5mm, yields a fall-off of -0.823 dB/mm (red line). The linear fit made to the second dataset, ranging from 1.58 mm to 3.58 mm, yields a fall-off of -1.841 dB/mm (green line).

The first set has a decay of $0.823\ dB/mm$ (red line), and the second set has a decay of $1.841\ dB/mm$ (green line). The remaining regression parameters are presented on table 6.

Table 6: Fit parameters for the two datasets, with 95% confidence bounds. These parameters were obtained using MATLAB.

	First Dataset (red)	**Second Dataset (green)**
Slope (dB/mm)	$-0.823\ (-0.931;\ -0.7149)$	$-1.841\ (-1.901;\ -1.782)$
$\mathbf{r^2}$	0.938	0.994

Experimentally, it was verified that the first set of data presents a decay of $0{,}46\ dB/mm$, and the last set has a decay of $3{,}02\ dB/mm$.[35]

In biomedical applications, the sensitivity fall-off of an OCT system should be less than 20 dB over a 2 mm ranging depth. The simulated sensitivity fall-off is within expected, and for the second dataset is better than the experimental value. However, many components of the SS-OCT system are not contemplated in this simulation, namely the optical ones (e.g. lenses and objectives). These components, as well as the fibre optics, introduce losses in the system that can compromise the performance of the SS-OCT system.

4.3.2 Axial Resolution Simulation

The axial resolution of the SS-OCT system is measured by determining the full width at half maximum ($FWHM$) of a Lorentz function fitted to the PSF.

In order to do so, the PSF for a mirror position of 30 µm was simulated and, using Origin Lab, a fit of a Lorentz function, described in equation (95), was made.

$$y = y_0 + \frac{2A}{\pi}\frac{\omega}{(x - x_c)^2 + \omega^2} \tag{95}$$

Here y_0 denotes the offset of the function, A is the area under the curve, x_c represents the center of the function, and ω indicates the FWHM. The height of the curve (H) can also be defined.

The graph represented on the following figure was obtained.

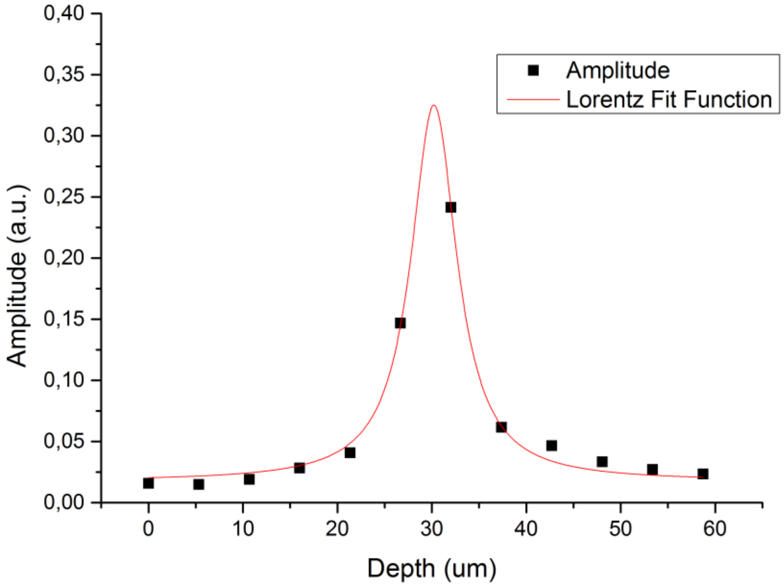

Figure 4.10 PSF of the SS-OCT system for a mirror position of 30 µm and respective fitted function.

The fit generated a Lorentz function with $FWHM = 5.95\,\mu m$. Therefore, the system's simulated axial resolution is $5.95\,\mu m$. A summary of the fit parameters is presented on table 7 and 8.

Table 7: Parameters of the fitted Lorentz function.

	Value	**Standard Error**
y0 (a.u.)	0.0175	0.0033
xc (µm)	30.23	0.1770
w (µm)	5.95	0.9405
A	2.874	0.1442
H	0.3077	0.0398

Table 8: Statistical value R^2 for the fitted Lorentz function.

Adjusted R-Square
0.9888

The theoretical value, calculated from equation (24), is $4.51\,\mu m$. This value is better than the simulated one, however it is calculated considering a source with a Gaussian spectrum. In reality, the spectrum's shape is far from Gaussian and therefore it is not expected to obtain the aforementioned value. The axial resolution depends greatly on the shape of the source's spectrum. For example, a system, whose source's power spectrum is rectangular, has an axial resolution given by $\Delta z = \frac{\pi}{\Delta k}$. [25] Hence, if we consider $\Delta k = 6.15 \times 10^5\, m^{-1}$, the axial resolution would be $\Delta z = 5.108\,\mu m$.

The axial resolution was experimentally calculated and a value of $8.8306\,\mu m$ was obtained. This value is worse than the simulated one, and since the axial resolution depends only on the source's characteristics, it should be improved.

4.3.3 Theoretical sample A-scan and minimum detectable signal

To simulate the three layered sample described in 4.1, the function $H[\omega]$ was defined as mentioned in the TD- and FD-OCT simulations, resulting in an array that was multiplied by the phase terms, following equations (91) and (92). The path length mismatch between the sample and reference arms was set to zero.

For the sake of clarity, the characteristics of the mentioned sample are listed again in table 9.

Table 9. Characteristics of a theoretical sample with three layers, as described in [1].

Layer j	**Refractive index n**	**Layer Thickness z (μm)**
1	1.00	5.00
2	1.30	15.00
3	1.50	30.00
4	1.00	0.00

The resulting SS-OCT interference signal is shown in figure 4.11, and the A-scan of the sample is presented in figure 4.12.

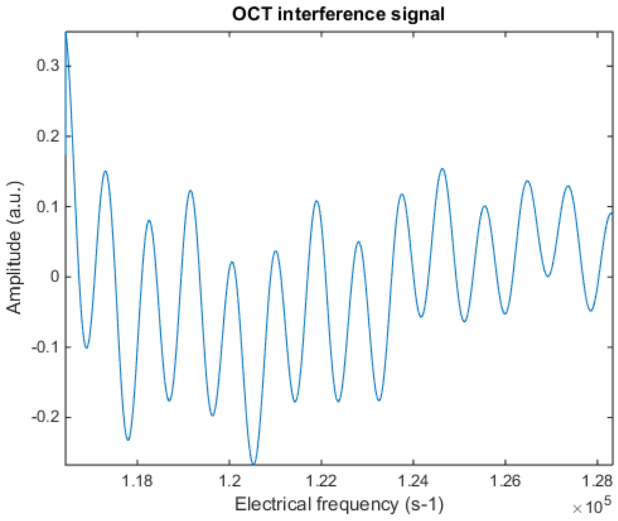

Figure 4.11 SS-OCT interference signal considering a sample with three layers. The signal is represented as a function of the electrical frequency.

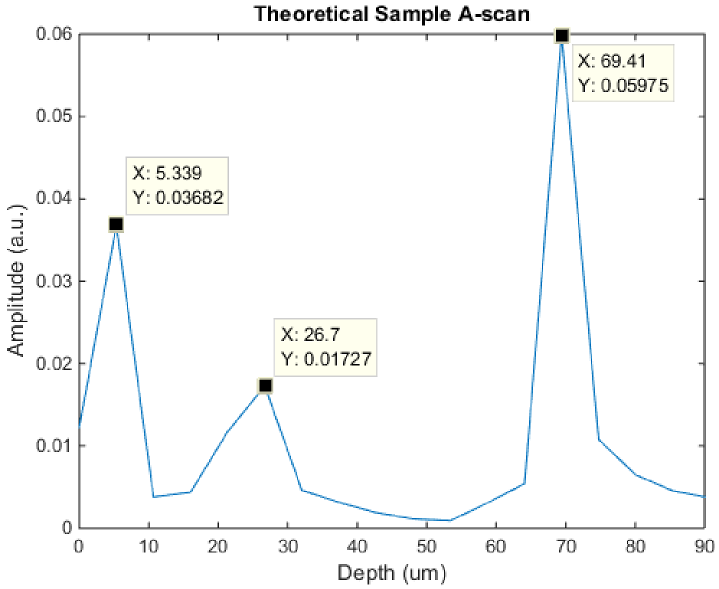

Figure 4.12 A-scan of the theoretical sample defined in 4.1, for the SS-OCT detection scheme. The three peaks corresponding to the sample's three layers can be identified: the first located at $x = 5.339\ \mu m$, the second located at $x = 26.7\ \mu m$, and the last located at $x = 69.41\ \mu m$.

The resulting A-scan presents the three expected amplitude peaks: the first located at $x_1 = 5.339\ \mu m$, the second located at $x_2 = 26.7\ \mu m$, and the third located at $x_3 = 69.41\ \mu m$. These results match the obtained results for the TD- and FD-OCT simulations.

A simulation to analyze the minimum possible difference between the refractive indices of two adjacent layers of the sample that create a detectable signal was performed. This was accomplished using the simulated sample shown in figure 4.12.

In a first experiment, the difference between the refractive indices of layers 1 (n_1) and 2 (n_2) was varied. n_1 was kept constant and n_2 varied. The position and amplitude (A_i) of the peaks were registered and table 10 was obtained.

Table 10. Refractive indices of the first and second layers of the theoretical sample. Simulated values of the peak position (depth) and amplitude. One should note that because n_2 varies, the position of its corresponding peak shifted.

First Layer			**Second Layer**		
n_1	Peak		n_2	Peak	
	Depth (µm)	A_1 (a.u.)		Depth (µm)	A_2 (a.u.)
1.00	5.339	0.0368	1.30	26.70	0.01726
	5.339	0.0320	1.25	21.36	0.01992
	5.339	0.0225	1.20	21.36	0.02894
	5.339	0.0237	1.15	21.36	0.0407
	5.339	0.0111	1.10	21.36	0.04632
	5.339	0.0065	1.05	21.36	0.04975
	5.339	-	1.03	21.36	0.05247

The ratio between the amplitudes of the peaks was graphically represented as a function of the difference between the refractive indices of the adjacent layers (Δn). Table 11 lists the calculated values for Δn and A_2/A_1. The graphical representation is shown in figure 4.13.

Table 11. Difference between the refractive indices of the first and second layers. Ratio between the amplitudes of the peaks.

$\boldsymbol{\Delta n = \lvert n_1 - n_2 \rvert}$	$\boldsymbol{A_2/A_1}$
0.30	0.47
0.25	0.62
0.20	1.29
0.15	1.72
0.10	4.17
0.05	7.69

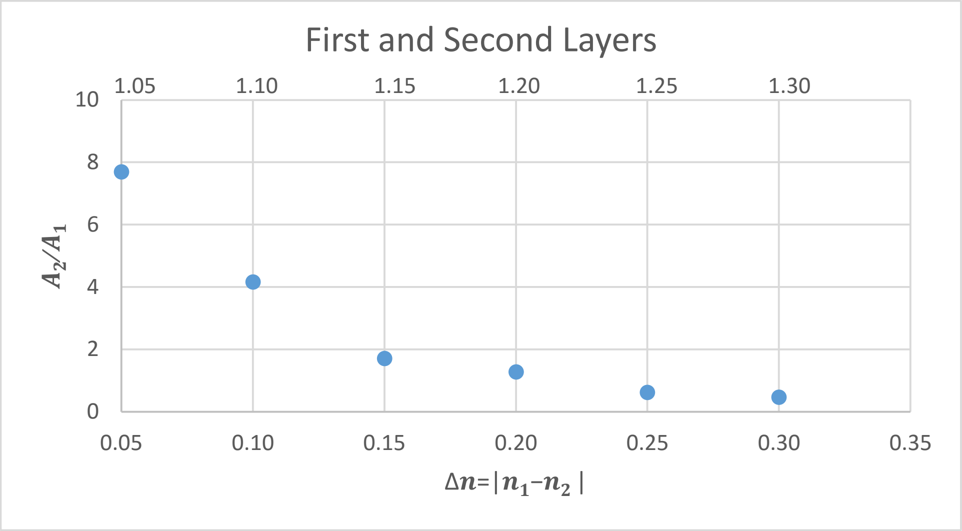

Figure 4.13: Graphic representation of A_2/A_1 vs. Δn. In the upper axis, the values of n_2 for each measurement are shown. In this experiment, n_1 was kept constant and n_2 varied from 1.3 to 1.05. For each n variation, we registered the amplitudes of the corresponding A-scan peaks and calculated the ratio between them. As the difference between the refractive index decreases, the ratio between the amplitude of the two peaks increases (i.e. the peak corresponding to the second layer has a much bigger amplitude than the peak corresponding to the first).

In the second experiment, the refractive index of layer 2 (n_2) was kept constant and the refractive index of layer 3 (n_3) was varied. The position and amplitude (A_i) of the peaks were registered and table 12 was obtained.

Table 12. Refractive indices of the second and third layers of the theoretical sample. Simulated values of the peak position (depth) and amplitude. One should note that because n_3 varies, the position of its corresponding peak shifted.

Second Layer			**Third Layer**		
n_2	Peak		n_3	Peak	
	Depth (µm)	A_2 (a.u.)		Depth (µm)	A_3 (a.u.)
1.30	26.70	0.01726	1.50	69.41	0.05974
	26.70	0.01369	1.45	69.41	0.04879
	26.70	0.01081	1.40	67.07	0.03563
	26.70	0.00818	1.39	67.07	0.03658
	26.70	0.00805	1.37	67.07	0.04179
	26.70	0.00654	1.35	67.07	0.04338
	26.70	0.00429	1.33	67.07	0.04245
	26.70	0.00231	1.31	67.07	0.03994

The ratio between the amplitudes of the peaks was graphically represented as a function of the difference between the refractive indices of the adjacent layers (Δn). Table 13 lists the calculated values for Δn and A_3/A_2. The graphical representation is shown in figure 4.14.

Table 13. Difference between the refractive indices of the second and third layers. Ratio between the amplitudes of the peaks.

$\boldsymbol{\Delta n = \lvert n_2 - n_3 \rvert}$	$\boldsymbol{A_3/A_2}$
0.20	3.46
0.15	3.56
0.10	3.30
0.09	4.47
0.07	5.19
0.05	6.63
0.03	9.90

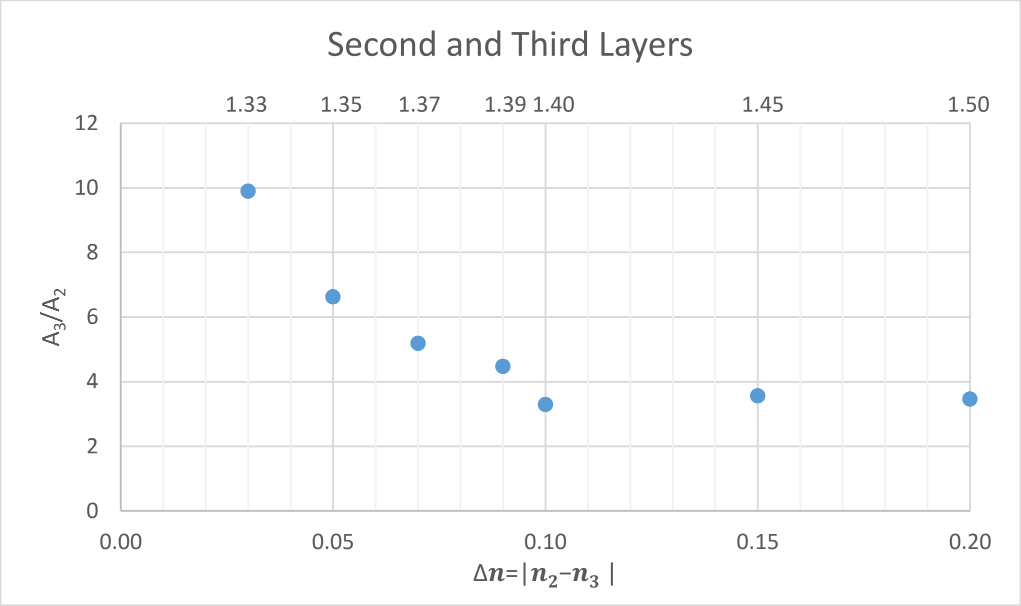

Figure 4.14: Graphic representation of A_3/A_2 vs. Δn. In the upper axis, the values of n_3 for each measurement are shown. In this experiment, n_2 was kept constant and n_3 varied from 1.33 to 1.50. For each n variation, we registered the amplitudes of the corresponding A-scan peaks and calculated the ratio between them. As the difference between the refractive index decreases, the ratio between the amplitude of the two peaks increases (i.e. the peak corresponding to the third layer has a much bigger amplitude than the peak corresponding to the second).

It is easily concluded from both experiments that when the difference between the refractive indices of two adjacent layers is zero, it is not possible to distinguish both peaks of the layers.

We concluded that it is not possible to clearly distinguish between two adjacent layers whose refractive indices have similar values. In both cases, as the difference between the refractive indices decreases, the amplitude of the first peak, whose refractive index remains constant, also decreases to a point where only the second peak is discernable. This happens because as the difference between the refractive indices of two adjacent layers diminishes, the reflectance of the interface, calculated by the Fresnel equations, also diminishes. Thus, the amplitude of the first peak will be smaller and more light will be transmitted to the second layer, which causes an increase in the amplitude of the second peak even if the reflectance between the second and the third layers diminishes. Furthermore, we consider that an A-scan peak is only detectable when its amplitude is superior to a threshold of three times the base line of the A-scan. So, in both experiments, it is not possible to detect the peak corresponding to the first layer, when Δn is equal or smaller than 0.1. Figures 4.15 and 4.16 illustrate this, by showing the A-scans for $\Delta n = 0.1$ and $\Delta n = 0.05$, of the two experiments.

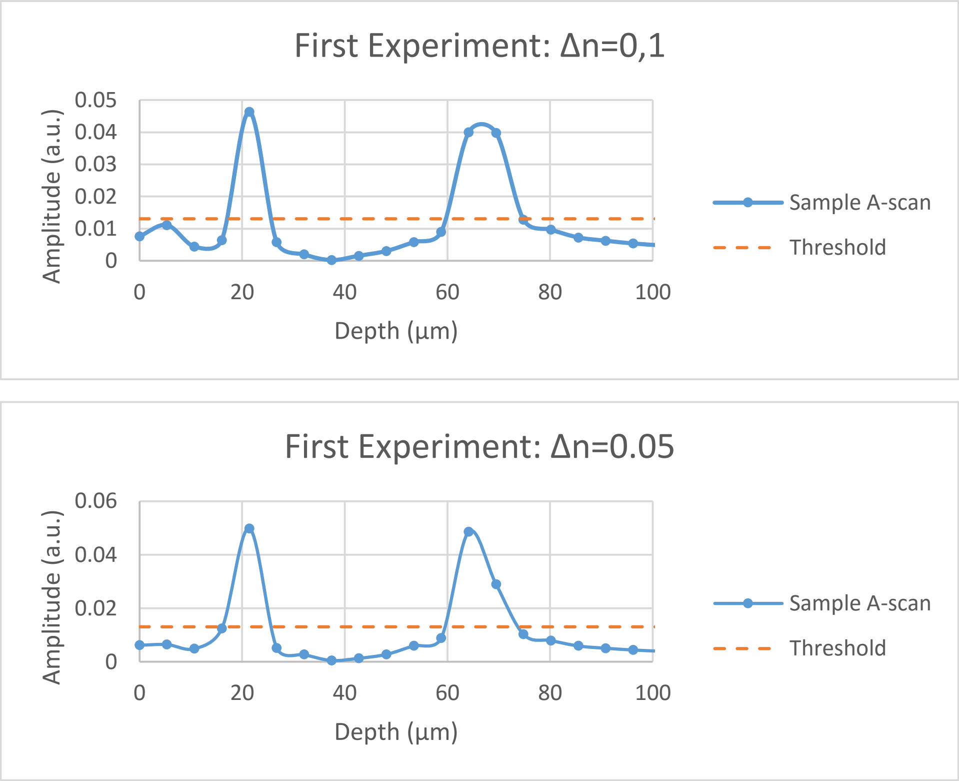

Figure 4.15 These graphs illustrate that for $\Delta n \leq 0.1$, it is not possible to detect the peak corresponding to the first layer, when we consider a threshold of three times the base line of the A-scan. Sample A-scan for $n_2 = 1.10$ (top) and $n_2 = 1.05$ (bottom). The remaining refractive indices were kept constant.

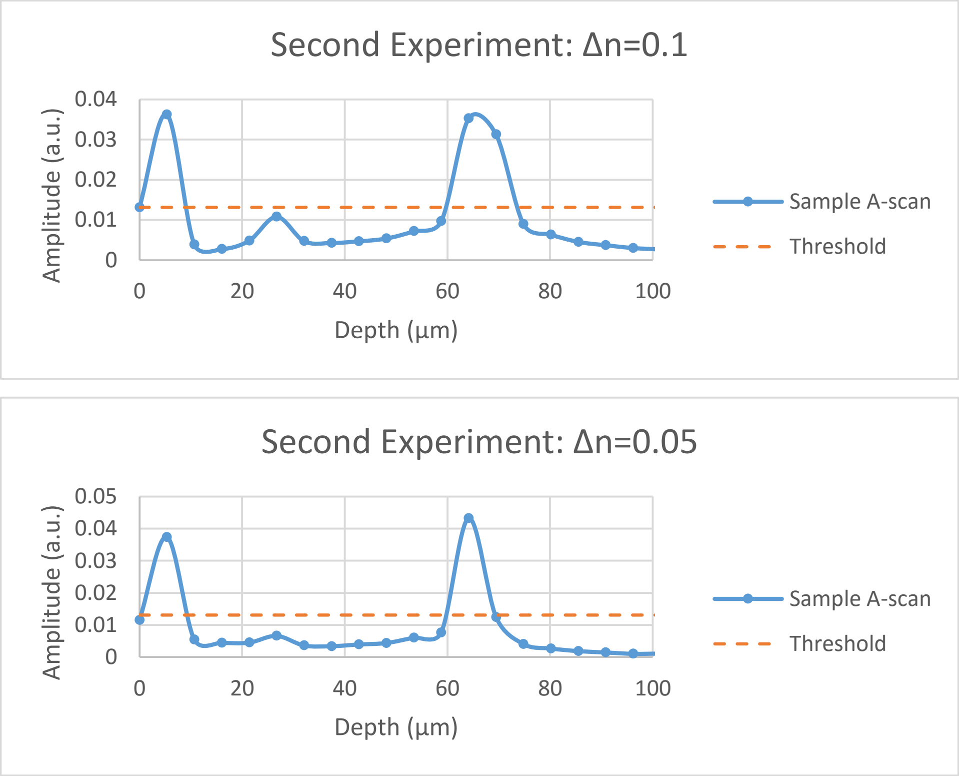

Figure 4.16 These graphs illustrate that for $\Delta n \leq 0.1$, it is not possible to detect the peak corresponding to the second layer, when we consider a threshold of three times the base line of the A-scan. Sample A-scan for $n_3 = 1.40$ (top) and $n_3 = 1.35$ (bottom). The remaining refractive indices were kept constant.

4.3.4 Glass coverslip simulation

The A-scan of a glass coverslip was simulated. It was considered that the material of the coverslip has a refractive index of $n = 1.5255$, and its thickness is approximately $0.13\,mm$. Following the simulation method described in 4.3, and setting the path length mismatch to zero, the interference signal and the A-scan shown in figures 4.17 and 4.18, respectively, were obtained. A peak located at $x = 1.98 \times 10^{-4}\,m = 0.198\,mm$ is expected at the simulated A-scan.

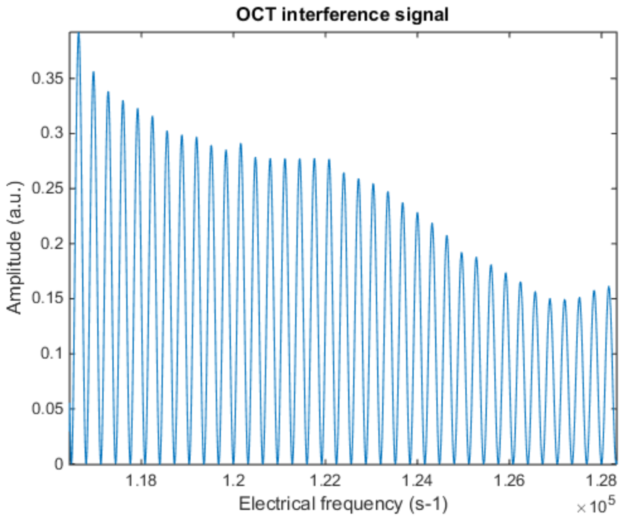

Figure 4.17 SS-OCT interference signal of a glass coverslip. The signal is represented as a function of the electrical frequency.

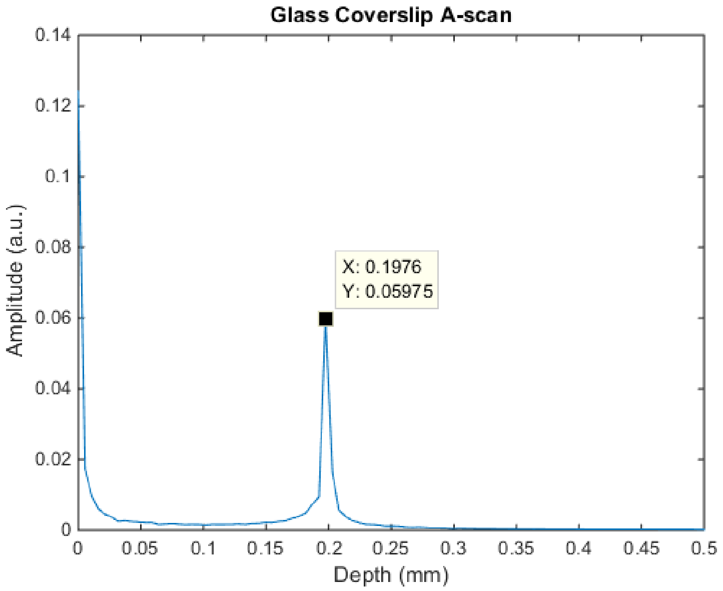

Figure 4.18 A-scan of a glass coverslip, for the SS-OCT detection scheme. A peak located at $x = 0.1976\ mm$ can be identified.

4.3.5 Small Animal Eye Model Simulation

The main goal of the SS-OCT in development at IBILI is to enable retinal imaging of small animals, such as rodents. Therefore, it is relevant to simulate theoretical models of the mouse and rat eyes.

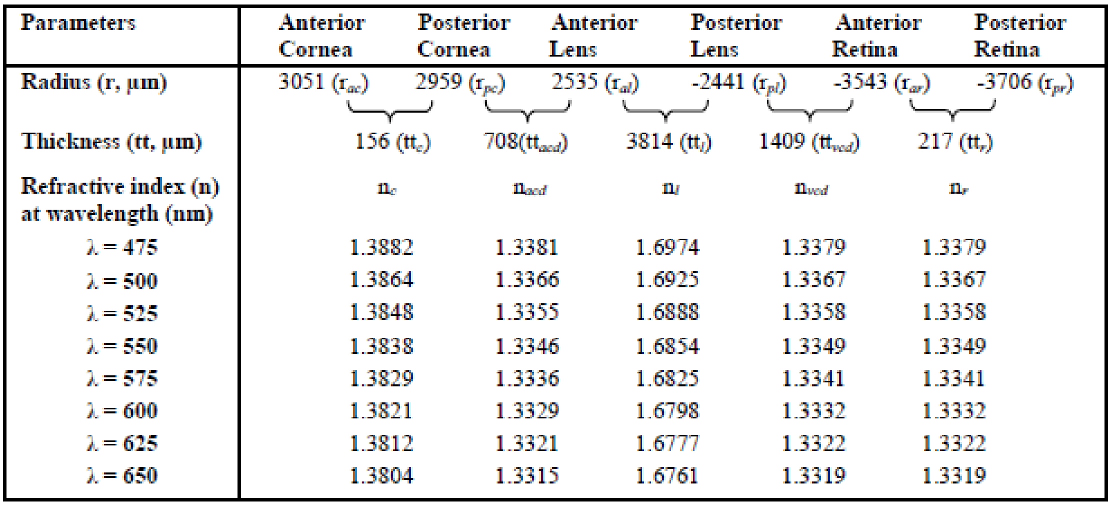

Parameters	Anterior Cornea		Posterior Cornea		Anterior Lens		Posterior Lens		Anterior Retina		Posterior Retina
Radius (r, µm)	3051 (r_{ac})		2959 (r_{pc})		2535 (r_{al})		-2441 (r_{pl})		-3543 (r_{ar})		-3706 (r_{pr})
Thickness (tt, µm)		156 (tt_c)		708(tt_{acd})		3814 (tt_l)		1409 (tt_{vcd})		217 (tt_r)	
Refractive index (n) at wavelength (nm)		n_c		n_{acd}		n_l		n_{vcd}		n_r	
$\lambda = 475$		1.3882		1.3381		1.6974		1.3379		1.3379	
$\lambda = 500$		1.3864		1.3366		1.6925		1.3367		1.3367	
$\lambda = 525$		1.3848		1.3355		1.6888		1.3358		1.3358	
$\lambda = 550$		1.3838		1.3346		1.6854		1.3349		1.3349	
$\lambda = 575$		1.3829		1.3336		1.6825		1.3341		1.3341	
$\lambda = 600$		1.3821		1.3329		1.6798		1.3332		1.3332	
$\lambda = 625$		1.3812		1.3321		1.6777		1.3322		1.3322	
$\lambda = 650$		1.3804		1.3315		1.6761		1.3319		1.3319	

Figure 4.19 Optical parameters for the optical model of the rat eye. Reproduced from [36].

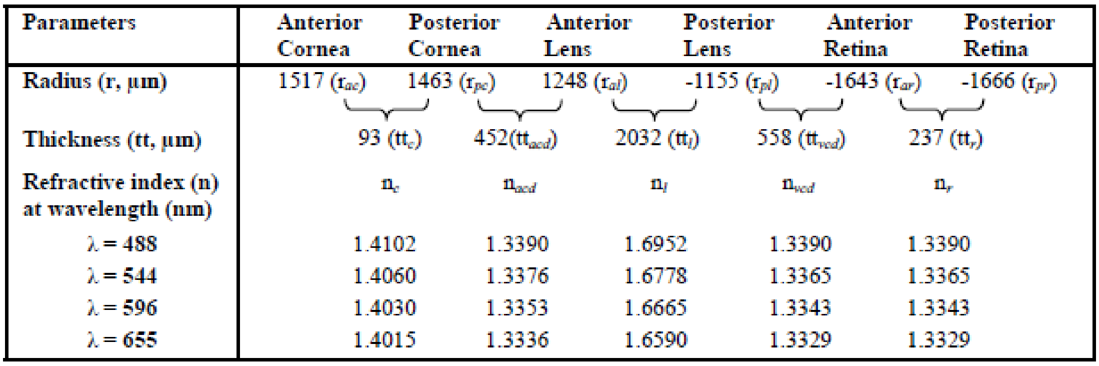

Parameters	Anterior Cornea		Posterior Cornea		Anterior Lens		Posterior Lens		Anterior Retina		Posterior Retina
Radius (r, µm)	1517 (r_{ac})		1463 (r_{pc})		1248 (r_{al})		-1155 (r_{pl})		-1643 (r_{ar})		-1666 (r_{pr})
Thickness (tt, µm)		93 (tt_c)		452(tt_{acd})		2032 (tt_l)		558 (tt_{vcd})		237 (tt_r)	
Refractive index (n) at wavelength (nm)		n_c		n_{acd}		n_l		n_{vcd}		n_r	
$\lambda = 488$		1.4102		1.3390		1.6952		1.3390		1.3390	
$\lambda = 544$		1.4060		1.3376		1.6778		1.3365		1.3365	
$\lambda = 596$		1.4030		1.3353		1.6665		1.3343		1.3343	
$\lambda = 655$		1.4015		1.3336		1.6590		1.3329		1.3329	

Figure 4.20 Optical parameters for the optical model of the mouse eye. Reproduced from [36].

To simulate the optical models, we considered the mean values of the refractive indices of each layer. However, in these models, there is no difference between the refractive indices of the two last layers. As verified in section 4.3.3, when the difference between the refractive indices of two adjacent layers is zero, it is impossible to distinguish the respective peaks.

The retina is a complex multilayered structure, with local variations of the refractive index. Therefore, for the purpose of this simulation, it was considered that the refractive index of the retina is 1.36.

The simulated parameters, i.e. layer thickness, and refractive index, are listed in tables 14 and 15.

Table 14. Simulated parameters of the rat eye optical model.

Layer	Refractive index n	Thickness z (μm)
Anterior Cornea – Posterior Cornea	1.384	156
Posterior Cornea – Anterior Lens	1.334	708
Anterior Lens – Posterior Lens	1.685	3814
Posterior Lens – Anterior Retina	1.335	1409
Anterior Retina – Posterior Retina	1.360	217

Table 15. Simulated parameters of the mouse eye optical model.

Layer	Refractive index n	Layer Thickness z (μm)
Anterior Cornea – Posterior Cornea	1.405	93
Posterior Cornea – Anterior Lens	1.336	452
Anterior Lens – Posterior Lens	1.675	2032
Posterior Lens – Anterior Retina	1.336	558
Anterior Retina – Posterior Retina	1.360	237

The simulated A-scans of the presented optical models should have five peaks each. The expected location of the peaks, for each eye model, is listed in the table below.

Table 16: Expected position of the A-scan peaks for the mouse and rat eye optical models.

	Peak Location (mm)	
Peak	**Mouse**	**Rat**
Anterior Cornea – Posterior Cornea	0.131	0.216
Posterior Cornea – Anterior Lens	0.735	1.160
Anterior Lens – Posterior Lens	4.138	7.587
Posterior Lens – Anterior Retina	4.878	9.468
Anterior Retina – Posterior Retina	5.200	9.763

The obtained A-scans are represented on figures 4.19 and 4.20.

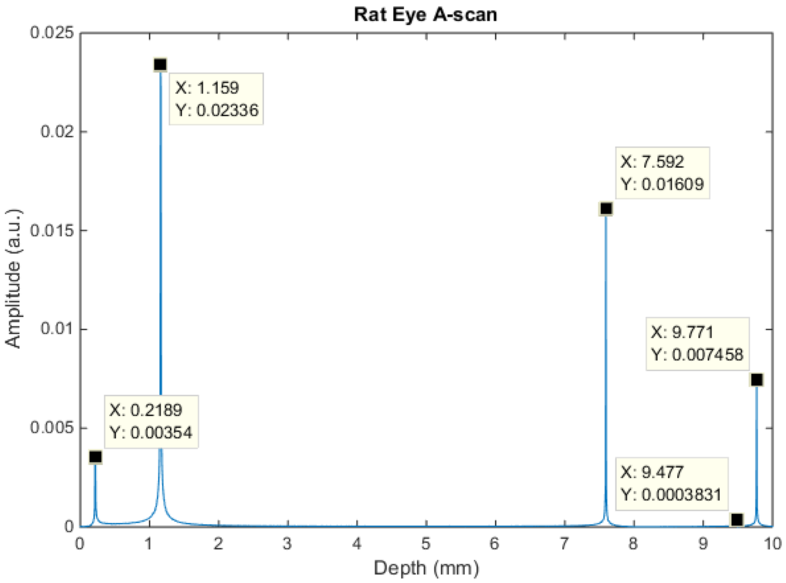

Figure 4.21 Simulated A-scan of the optical model of the rat eye. Five peaks can be distinguished: the first located at 0.2136 mm, the second at 1.159 mm, the third at 7.592 mm, the fourth at 9.477 mm, and the last at 9.771 mm.

There are five discernable peaks at the simulated rat eye A-scan. The peaks appear at $x_1 = 0.2136\,mm$, $x_2 = 1.159 mm$, $x_3 = 7.592\,mm$, $x_4 = 9.477\,mm$, and $x_5 = 9.771\,mm$.These values are in line with the expected ones.

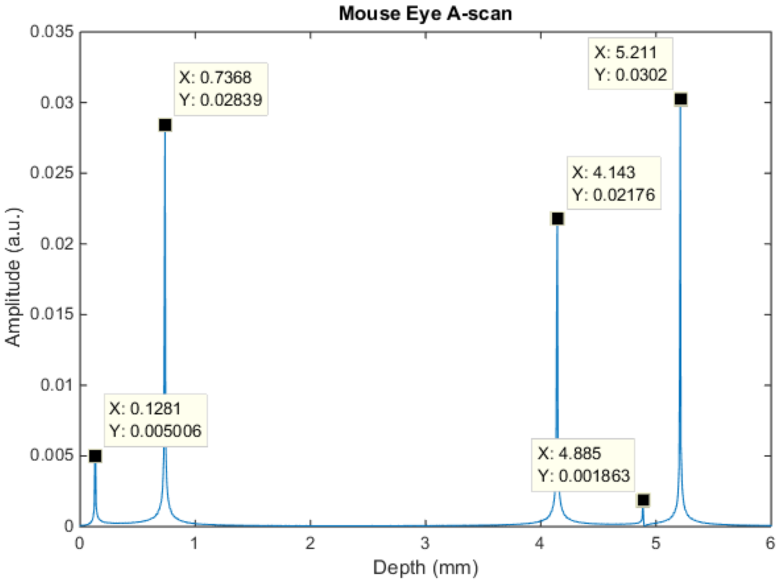

Figure 4.22 Simulated A-scan of the optical model of the mouse eye. Five peaks can be distinguished: the first located at 0,1281 mm, the second at 0,7368 mm, the third at 4,143 mm, the fourth at 4,885 mm, and the last at 5,211 mm.

In the A-scan of the mouse eye, the five expected peaks can be distinguished. The first three peaks, corresponding to the first three layers, are located at $x_1 = 0.1218\ mm$, $x_2 = 0.7368\ mm$, and $x_3 = 4.143\ mm$. The last two peaks are located at $x_4 = 4.885\ mm$ and $x_5 = 5.211\ mm$ The obtained peak positions are close to the expected positions.

It should be noted that this simulation was performed setting the number of samples N to a much higher value than the actual value of the SS-OCT system ($N_{real} = 1376$ samples). By doing this, the maximum achievable depth is greater than the actual one ($z_{max,real} = 3.51\ mm$ vs. $z_{max,sim} = 10.9\ mm$). This allows to obtain accurate A-scans of the rat and mouse eye models. If N is set to 1376, the positions of the expected peaks in the A-scan appears shifts, as shown in the figures below.

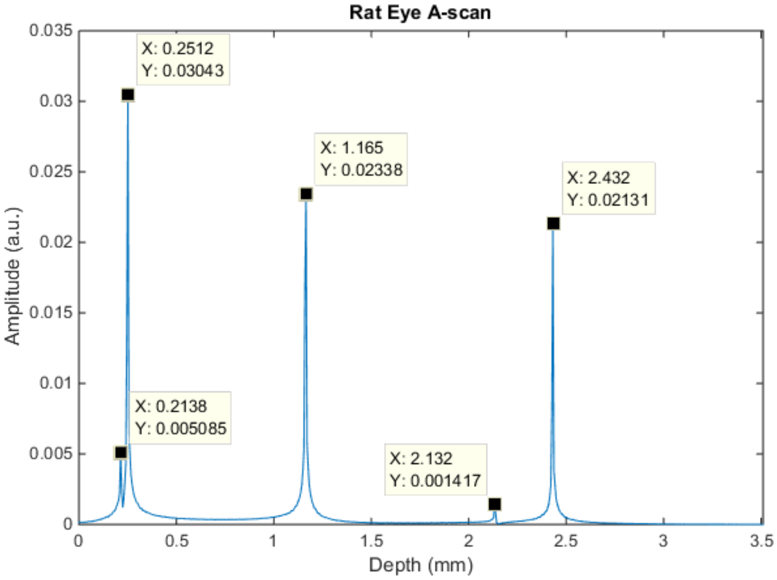

Figure 4.23 Simulated A-scan of the optical model of the rat eye, with $N = 1376$. Five peaks can be distinguished: the first located at 0.2138 mm, the second at 0.2512 mm, the third at 1.165 mm, the fourth at 2.132 mm, and the last 2.432 mm. The shift in the position of the peaks due to the difference in the maximum depth is noticeable.

The five expected peaks appear at different positions. The first peak is located at $x_1 = 0.2138\, mm$, the second is at $x_2 = 0.2512\, mm$, the third is located at $x_3 = 1.165\, mm$, the fourth is at $x_4 = 2.132\, mm$, and the last is at $x_5 = 2.432\, mm$.

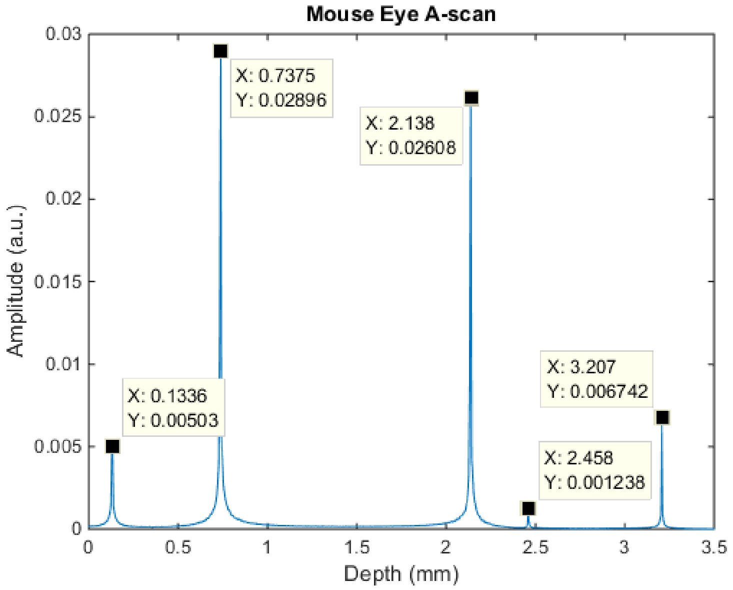

Figure 4.24 Simulated A-scan of the optical model of the mouse eye, with $N = 1376$. Five peaks can be distinguished: the first located at 0.1336 mm, the second at 0.7375 mm, the third at 2.138 mm, the fourth at 2.458 mm, and the last at 3.207 mm. The shift in the position of the peaks due to the difference in the maximum depth is noticeable.

In the A-scan of the mouse eye model, the first peak is located at $x_1 = 0.1336\,mm$, the second is at $x_2 = 0.7375\,mm$, the third is located at $x_3 = 2.138\,mm$, the fourth is at $x_4 = 2.458\,mm$, and the last is at $x_5 = 3.207\,mm$. The first two peaks are still at a position close to the expected one.

However, the SS-OCT system doesn't aim to acquire the entire length of the rodent's eye. It works by focusing specific ocular structures and obtaining their accurate A-scans. Considering this, we simulated the optical model of the mouse retina.

The retina is a multi-layered structure, with variations of the refractive indices from one layer to the other. Following [37], we considered the mouse retina to be constructed by the following layers: retinal nerve fibre, inner nucleus, outer plexiform, outer nucleus, external limiting membrane, retinal pigmented epithelium and outer retina. Figure 4.25 shows a B-scan of the mouse retina, where the different sublayers are discriminated.

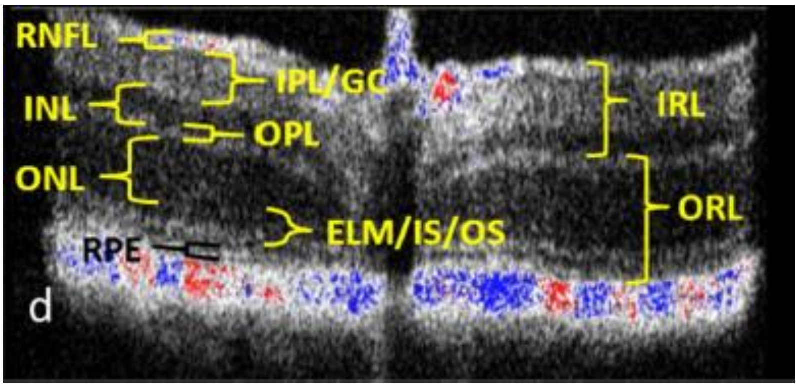

Figure 4.25 B-scan of the retina of a mouse, showing the different sublayers, namely: retinal nerve fibre layer (RNFL), Inner Nuclear Layer (INL), Outer Plexiform Layer (OPL), Outer Nuclear Layer (ONL), External Limiting Membrane (ELM), and Retinal Pigmented Epithelium (RPE). Other substructures, which were not simulated, are also shown. Reproduced from [37].

In table 17, the simulated parameters for layer thickness and refractive index are listed. This model was made taking into account the information in [37] and [38].

Table 17. Simulated parameters of the mouse retina optical model.

Layer	Refractive index n	Thickness z (μm)
Vitreous	1.335	-
Retinal nerve fibre	1.369	19.12
Inner Nucleus	1.376	59.62
Outer Plexiform	1.370	27.82
Outer Nucleus	1.383	62.80
External Limiting Membrane	1.379	26.04
Retinal Pigmented Epithelium	1.368	18.23
Outer Retina	1.333	-

The resulting simulated A-scan is shown in figure 4.26.

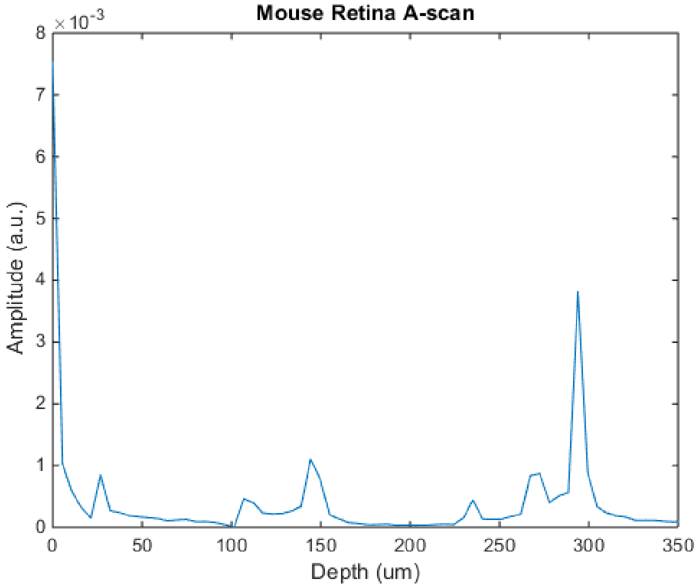

Figure 4.26 Simulated A-scan of the mouse retina optical model, with $N = 1376$. There are six peaks located at 26.72 µm, 106.9 µm, 144.3 µm, 235.2 µm, 267.2 µm, and 293.9 µm.

The expected position of the peaks, as well as the simulated position, are presented in table 18.

Table 18. Expected and simulated positions of the A-scan peaks.

Peak	Expected Position (μm)	Simulated Position (μm)
Vitreous – RNFL	0	0
RNFL – INL	26.175	26.72
INL – OPL	108.21	106.9
OPL – ONL	146.33	144.3
ONL – ELM	233.18	235.2
ELM – RPE	269.09	267.2
RPE – Outer Retina	294.03	293.9

The simulated peak positions are close to the expected ones, despite some deviations of the values.

5. CONCLUSIONS AND FUTURE DIRECTIONS

The main goal of this work was to simulate the layout of the Swept-Source OCT system in development at IBILI and some of its crucial parameters, namely the sensitivity fall-off and the axial resolution. Optical models of samples, such as a glass coverslip and rodent’s eyes, were also simulated.

In the present chapter, the results are discussed, and the limitations of the work are addressed. Finally, an analysis of possible future work is made.

5.1 DISCUSSION OF THE FINAL RESULTS

Regarding the sensitivity fall-off simulation, it was verified that in a depth range from 20 µm to 1.5 mm the peak sensitivity decays $0.823\ dB/mm$. From 1.5 mm to 3.58 mm, the peak sensitivity has a decay of $1.841\ dB/mm$. Experimentally, the fall-off measurements yielded a fall-off of $0.46\ dB/mm$ for the first depth range, and of $3.02\ dB/mm$ for the second. For biomedical imaging, an SS-OCT system is expected to present a fall-off of 20 dB over a 2 mm depth range. Both the simulated and experimental values are within the requirements posed by biomedical imaging.

There are three major contributions for the sensitivity fall-off of an SS-OCT system: the decrease in the visibility of higher fringe frequencies for higher imaging depth; the electronic fall-off that results from the finite bandwidth of the balanced amplifier; and the depth of focus defined by the optical components. Our simulation only considers the first two contributions. This may explain why the simulates fall-off in the depth range from 1.5 mm to 3.58 mm is better than the value measured experimentally.

Concerning the axial resolution, the simulation yielded a result of approximately $6\ \mu m$, while the experimental results were close to $9\ \mu m$. The required axial resolution, for biomedical imaging, must be less than $10\ \mu m$ and theoretically, for a source with a Gaussian spectrum, with 1060 nm centre wavelength and 101 nm bandwidth, it has a value of $4.51\ \mu m$. However, the actual power spectrum of the Axsun Swept Source Engine is not Gaussian. Therefore, the actual value of the axial resolution must be worse than the $4.51\ \mu m$ value obtained for a

Gaussian source.

Finally, because this parameter only depends on the centre wavelength and bandwidth of the source, the actual value of the system's axial resolution should be optimized to a value closer to the simulated.

We also simulated the minimum possible difference between the refractive indices (Δn) of two adjacent layers that produces a detectable signal. As expected, when the two layers have refractive indices whose value is equal or close, it is not possible to distinguish both peaks on the sample's A-scan. If we set a threshold detection value equal to three times the noise level of an average A-scan, we conclude that the minimum detectable refractive index difference is 0.1.

The simulation of the optical models of the mouse and rat's eye, showed that the SS-OCT system is not capable of producing A-scans of the entire length of the rodent's eyes. Due to the number of acquired samples ($N_{real} = 1376$ samples), the maximum achievable depth of the system is of 3.51 mm. Therefore, the A-scan peaks corresponding to the different layers appear in different positions than the expected. However, the goal of the SS-OCT system is to focus on specific ocular structures and obtain their accurate representations. This goal can be achieved. In fact, when we consider only the multilayered model of the retina, the simulated A-scan presents all the expected peaks at the right positions.

The performed simulations also included the electronic noise associated with the balanced photodetector. It was concluded that it doesn't have a significant impact on the results, i.e. the signal is not degraded due to the photodetector noise.

It is important to note that the optical components of the SS-OCT system, namely the objective lenses, are not simulated. The simulation includes only the swept-source engine, the fibre optic couplers, and the balanced photodetector. This is a clear limitation of the work because the optical components introduce losses on the system and are responsible for defining the system depth of focus. This optical effect contributes to the sensitivity fall-off and may explain the higher fall-off observed experimentally, when compared with the simulation results, for the depth range between 1.5 mm and 3.58 mm.

Furthermore, the simulation doesn’t account for absorption and scattering within the sample. These phenomena, as well as dispersion and attenuation on the optical fibres, lead to power losses that affect the final results.

5.2 FUTURE WORK

In the future, the layout simulations can be further explored in order to determine all the performance limitations of the system and identify possible bottlenecking associated with the components.

Therefore, it is important to fully characterize and simulate the following components: collimators, objectives and optical fibres. This study of light propagation would allow to identify system limitations related to attenuation and dispersion and consequently implement solutions to overcome them.

It would also be interesting to improve the simulation of the sample's response so that the interaction of light with the sample structures (scattering and absorption phenomena) is described.

REFERENCES

[1] P. H. Tomlins and R. K. Wang, “Theory, developments and applications of optical coherence tomography,” *J. Phys. D. Appl. Phys.*, vol. 38, no. 15, pp. 2519–2535, Aug. 2005.

[2] M. Wojtkowski, “High-speed optical coherence tomography: basics and applications,” *Appl. Opt.*, vol. 49, no. 16, pp. D30–D61, 2010.

[3] P. Serranho, M. Morgado, and R. Bernardes, “Optical Coherence Tomography: A Concept Review,” in *Optical Coherence Tomography*, R. Bernardes and J. Cunha-Vaz, Eds. Springer-Verlag Berlin Heidelberg, 2012, pp. 139–156.

[4] B. Potsaid, B. Baumann, D. Huang, S. Barry, A. E. Cable, J. S. Schuman, J. S. Duker, and J. G. Fujimoto, “Ultrahigh speed 1050nm swept source/Fourier domain OCT retinal and anterior segment imaging at 100,000 to 400,000 axial scans per second,” *Opt. Express*, vol. 18, no. 19, pp. 20029–20048, 2010.

[5] A. F. Fercher, W. Drexler, C. K. Hitzenberger, and T. Lasser, “Optical coherence tomography — principles and applications,” *Rep. Prog. Phys.*, vol. 66, no. 66, pp. 239–303, 2003.

[6] J. Fujimoto and W. Drexler, “Introduction to Optical Coherence Tomography,” in *Optical Coherence Tomography - Technology and Applications*, J. Fujimoto and W. Drexler, Eds. Springer, 2008, pp. 1 – 45.

[7] J. . Izatt and M. A. Choma, “Theory of optical coherence tomography,” in *Optical Coherence Tomography - Technology and Applications*, W. Drexler and J. G. Fujimoto, Eds. Springer, 2008, pp. 47–72.

[8] J. G. Fujimoto, “Optical Coherence Tomography: Introduction,” in *Handbook of Optical Coherence Tomography*, B. E. Bouma and G. J. Tearney, Eds. Marcel Dekker, Inc., 2002, pp. 1–40.

[9] J. M. Schmitt, “Optical coherence tomography (OCT): a review,” *IEEE J. Sel. Top. Quantum Electron.*, vol. 5, no. 4, pp. 1205–1215, 1999.

[10] B. E. Bouma and G. J. Tearney, “Optical Sources,” in *Handbook of Optical Coherence Tomography*, B. E. Bouma and G. J. Tearney, Eds. Marcel Dekker, Inc., 2002, pp. 67–97.

[11] R. Paschotta, “Coherence,” *Encyclopedia of Laser Physics and Technology*, 2008. [Online]. Available: https://www.rp-photonics.com/coherence.html. [Accessed: 29-Aug-2015].

[12] P. Jansz, S. Richardson, G. Wild, and S. Hinckley, “Modeling of low coherence interferometry using broadband multi-gaussian light sources,” *Photonic Sensors*, vol. 2, no. 3, pp. 247–258, 2012.

[13] A. Z. De Freitas, M. M. Amaral, and M. P. Raele, “Optical Coherence Tomography : Development and Applications.,” in *Laser Pulse Phenomena and Applications*, D. F. J. Duarte, Ed. InTech, 2010, pp. 409–432.

[14] A. G. Podoleanu, “Optical coherence tomography.,” *Br. J. Radiol.*, vol. 78, no. 935, pp. 976–988, 2005.

[15] S. H. Yun and B. E. Bouma, “Wavelength Swept Lasers,” in *Optical Coherence Tomography - Technology and Applications*, W. Drexler and J. G. Fujimoto, Eds. Springer, 2008, pp. 359–377.

[16] D. P. Popescu, L. P. I. Choo-Smith, C. Flueraru, Y. Mao, S. Chang, J. Disano, S. Sherif, and M. G. Sowa, “Optical coherence tomography: Fundamental principles, instrumental designs and biomedical applications,” *Biophys. Rev.*, vol. 3, no. 3, pp. 155–169, 2011.

[17] H. D. Ford, R. Beddows, P. Casaubieilh, and R. P. Tatam, “Comparative signal-to-noise analysis of fibre-optic based optical coherence tomography systems,” *J. Mod. Opt.*, vol. 52, no. 14, pp. 1965–1979, Sep. 2005.

[18] M. H. Frosz, M. Juhl, and M. H. Lang, “Optical Coherence Tomography : System Design and Noise Analysis,” Roskilde, 2001.

[19] C. C. Rosa and A. G. Podoleanu, “Limitation of the achievable signal-to-noise ratio in optical coherence tomography due to mismatch of the balanced receiver,” *Appl. Opt.*, vol. 43, no. 25, pp. 4802–4815, 2004.

[20] J. F. de Boer, “Spectral/Fourier Domain Optical Coherence Tomography,” in *Optical Coherence Tomography - Technology and Applications*, W. Drexler and J. G. Fujimoto, Eds. Springer, 2008, pp. 147–157.

[21] B. E. Bouma, G. J. Tearney, B. J. Vakoc, and S. H. Yun, “Optical Frequency Domain Imaging,” in *Optical Coherence Tomography - Technology and Applications*, W. Drexler and J. G. Fujimoto, Eds. Springer, 2008, pp. 209–237.

[22] J. Xi, L. Huo, J. Li, and X. Li, “Generic real-time uniform K-space sampling method for high-speed swept-source optical coherence tomography.,” *Opt. Express*, vol. 18, no. 9, pp. 9511–9517, 2010.

[23] S. Chang, Y. Mao, and C. Flueraru, “Dual-source swept-source optical coherence tomography reconstructed on integrated spectrum,” *Int. J. Opt.*, vol. 2012, no. 1, pp. 0–5, 2012.

[24] M. a. Choma, K. Hsu, and J. a. Izatt, “Swept source optical coherence tomography using an all-fiber 1300-nm ring laser source,” *J. Biomed. Opt.*, vol. 10, no. 4, p. 044009, 2005.

[25] M. Choma, M. Sarunic, C. Yang, and J. Izatt, “Sensitivity advantage of swept source and Fourier domain optical coherence tomography.,” *Opt. Express*, vol. 11, no. 18, pp. 2183–2189, 2003.

[26] T. Wu, Z. Ding, L. Wang, and M. Chen, “Spectral phase based k-domain interpolation for uniform sampling in swept-source optical coherence tomography.,” *Opt. Express*, vol. 19, no. 19, pp. 18430–9, 2011.

[27] M. Wojtkowski, R. Leitgeb, A. Kowalczyk, T. Bajraszewski, and A. F. Fercher, “In vivo human retinal imaging by Fourier domain optical coherence tomography.,” *J. Biomed. Opt.*, vol. 7, no. 3, pp. 457–463, 2002.

[28] R. Huber, M. Wojtkowski, and J. G. Fujimoto, “Fourier Domain Mode Locking (FDML): A new laser operating regime and applications for optical coherence tomography,” *Opt. Express*, vol. 14, no. 8, 2006.

[29] M. R. Hee, “Optical Coherence Tomography: Theory,” in *Handbook of*

Optical Coherence Tomography, B. E. Bouma and G. J. Tearney, Eds. Marcel, 2002, pp. 41–66.

[30] A.-H. Z. Dhalla, “Development of Extended-Depth Swept Source Optical Coherence Tomography for Applications in Ophthalmic Imaging of the Anterior and Posterior Eye,” Doctoral Thesis, Duke University, 2012.

[31] “Axsun OCT Swept Source Engine Operators’ Manual.” Axsun Technologies, Massachusetts, USA, 2010.

[32] “Balanced Amplified Photodetectors: PDB47xC Operation Manual.” Thorlabs, pp. 1–30, 2014.

[33] “1064 nm, Single Mode Fused Fiber Optic Couplers / Taps,” *Thorlabs, Inc*, 2015. [Online]. Available: http://www.thorlabs.com/newgrouppage9.cfm?objectgroup_id=8465. [Accessed: 03-Jun-2015].

[34] W. Wieser, B. R. Biedermann, T. Klein, C. M. Eigenwillig, and R. Huber, “Multi-megahertz OCT: High quality 3D imaging at 20 million A-scans and 4.5 GVoxels per second.,” *Opt. Express*, vol. 18, no. 14, pp. 14685–14704, 2010.

[35] J. M. de A. Rodrigues, “Optical Coherence Tomography: High Rate Acquisition Setup, Image Processing and Parallelism,” Master Thesis, Universidade de Coimbra, 2015.

[36] G. Bawa, T. V Tkatchenko, I. Avrutsky, and A. V Tkatchenko, “Variational analysis of the mouse and rat eye optical parameters.,” *Biomed. Opt.*

Express, vol. 4, no. 11, pp. 2585–95, Jan. 2013.

[37] L. R. Ferguson, J. M. Dominguez II, S. Balaiya, S. Grover, and K. V. Chalam, “Retinal Thickness Normative Data in Wild-Type Mice Using Customized Miniature SD-OCT,” *PLoS One*, vol. 8, no. 6, pp. 1–8, 2013.

[38] A. Ajo, “On the refractive index of the retina.,” *Acta Physiol. Scand.*, vol. 13, no. 1–2, pp. 130–49, 1947.

APPENDIX A

SOURCE CODE FOR THE SIMULATION OF THE BASIC OCT SETUP BASED ON A MICHELSON INTERFEROMETER

```
% constants
c = 3.00e+08;

% gaussian source
lc = 800e-09;
l = linspace(lc-(lc/3), lc+(lc/3), 1024);
fwhm = 50e-09;
sigma = fwhm./sqrt(8*log(2));

wc = (2*pi*c)/lc;
w = linspace(wc-(wc/3), wc+(wc/3), 1024);
fwhm_w = (2*pi*c*fwhm)./(lc.^2);
sigma2 = fwhm_w./sqrt(8*log(2));

y = gaussmf(w, [sigma2, wc]);

figure (), plot (w, y), axis tight, title ('Light Source Spectrum')
xlabel ('Optical Frequency (rad.s-1)'), ylabel ('Amplitude (a.u.)')


% sample

n = [1.00 1.30 1.50 1.00];
z = [5.00e-06 15.00e-06 30.00e-06 0.00e-06];

s1 = 0;
h = 0;

for i = 1:3
    rj = (n(i+1)-n(i))/(n(i+1)+n(i));
    s1 = s1 + n(i)*z(i);
    h = h + rj*exp(1i*2.*(w./c)*s1);
end


% time domain

x = linspace (0, 100e-6, 1024);
T1 = zeros(size(x));

for j = 1:length(x)
    for jj = 1:length(w)
        ph = cos(2*x(j)*w(jj)/c);
        T1(j) = T1(j) + real(0.5*(y(jj)*h(jj)*ph));
    end
end
```

```
figure (), plot(x./1e-6, T1), axis tight, title ('TD-OCT Interferogram')
xlabel ('Mirror displacement (um)'), ylabel ('Amplitude (a.u.)')


% fourier domain

for j=1:length(w)
    I(j) = (0.25*y(j).*(abs(h(j)).^2))+(0.25*y(j))+(0.5*real(y(j)*h(j)));
end

N = length(I);
I2 = abs(fftshift(ifft(I)));
I2 = fliplr(I2(1,1:N/2));
wrange= w(1,length(w))-w(1,1);
zz = linspace(0,(N*pi*c)/(2*1.*wrange),N/2);

figure(), plot(w, I), title ('FD-OCT: Spectral Intensity')
xlabel('Optical Frequency (rad.s-1)'), ylabel('Amplitude (a.u.)')
xlim([2.1e15 2.6e15])

figure(), plot(zz./1e-6, I2), title('FD-OCT: A-scan')
xlabel('Depth (um)'), ylabel('Amplitude (a.u.)')
xlim([0 100])
```

APPENDIX B

SOURCE CODE FOR THE SIMULATION OF THE SWEPT-SOURCE OC SYSTEM LAYOUT

```
%% Constants
c = 3.00e+08;
R = 0.72; % Responsivity of the photodetector
G = 10e4; % Transimpedance gain of the photodetector
B = 400e6;  % Photodetector bandwidth
% Sweep frequency of the source
fsweep = 100e3; % Source’s sweep frequency
vsweep = (101e-9)*fsweep; % Source’s sweep velocity

%% Source Power Spectrum
filename = 'espectro2.xlsx';
sheet = 2;
x_range = 'A2:A36';
y_range = 'B2:B36';

wavelength = xlsread(filename, sheet, x_range); % Wavelength (nm)
l = wavelength.*1e-9; % Wavelength (m)

power = xlsread(filename, sheet, y_range); % Power (dBm)
power2 = flip (power);
power2 = db2pow(power2); % Power (W)

w = 2*pi*c./l; % Optical frequency
w = flip(w);

%% Spectrum interpolation
% Linearly spaced w vector
ww = linspace(2*pi*c./(1090e-9), 2*pi*c./(989e-9), 1376);
vq = interp1(w, power2, ww, 'pchip'); % Interpolation

lc = 1060e-09; % centre wavelength
fwhm = 101e-09;
wcentral = (2*pi*c)/lc;

delta_w = ww(2)-ww(1);
sigma_w = delta_w/2;
wwrange= ww(1,length(ww))-ww(1,1);

f = 2*vsweep*ww./c; % Electrical Frequency
fcentral = 2*vsweep*wcentral./c;
delta_f = f(2)-f(1);

%% Sample
% Glass Coverslip
% n = [1.00 1.5255 1.00];
% z = [0.00 0.13e-3 0.00];
% Theoretical sample as described by Tomlins
% n = [1.00 1.3 1.4 1.00];
% z = [5.00e-06 15.00e-06 30.00e-06 0.00e-06];

% Mouse eye model
n = [1.405 1.336 1.675 1.336 1.360 1.00];
z = [93e-06 452e-06 2032e-06 558e-06 237e-06 0];
% Rat eye model
% n = [1.384 1.334 1.685 1.335 1.360 1.00];
% z = [156e-06 708e-06 3814e-06 1409e-06 217e-06 0];

% mouse retina: vitreous(lens-retina)-retinal nerve fiber-inner nuclear-outer
% plexiform-outer nuclear-external limiting membrane-retinal pigmented
% epitelium-outer
% n = [1.335 1.369 1.376 1.370 1.383 1.379 1.368 1.333];
% z = [0 19.12e-6 59.62e-6 27.82e-6  62.80e-6   26.04e-6   18.23e-6   0];

s = 0;
h = 0;

for j = 1:(length(n)-1)
    rj = (n(j+1)-n(j))/(n(j+1)+n(j));
    s = s + n(j)*z(j);
    h = h + rj*exp(1i*2*(ww./c)*s);
end

%% OCT Signal

dz = 0e-6; % path length mismatch

% Phase Accumulation
% phi = exp(-1i*((2*dz(j2).*ww)./c));
phi = exp(-1i*(dz.*(f./vsweep))); % as a function of electrical frequency

% Signal Fall-Off
% delta_tau = (2*dz(j2)./c).^2;
% sigma_tau = (1/(sigma_w.^2));
% tau = exp(-delta_tau./(2*sigma_tau));
tau = exp(-((dz./vsweep).^2)*(delta_f.^2)*(1/8)); % as a function of electrical
frequency

%% Balanced Detector

Ps = (10.^(-0.66/10))*(10.^(-3.78/10))*(10.^(-3.15/10)); % sample power loss due to the
couplers
Pr = (10.^(-3.15/10))*(10.^(-3.78/10))*(10.^(-10.25/10)) ; % reference power loss due to
the coupler

A_s = sqrt(0.901*0.536*0.536).*vq.*Ps; % Amplitude of the sample beam
A_r = sqrt(0.099*0.464*0.464).*vq.*Pr; % Amplitude of the reference beam
A_rec = A_r+A_s; % Amplitude of the recombined beam

% Beam splitting at the last 50:50 coupler
Pp = 10.^((-(3.15+3.78))./10); % power loss

A1 = sqrt(0.536).*A_rec.*Pp; % amplitude 1
A2 = sqrt(0.464).*A_rec.*Pp; % amplitude 2
```

```
I1 = real(A1.*phi.*tau.*h); % optical input 1
I2 = real(A2.*phi.*tau.*h); % optical input 2
% h is substituted by the reflectivity of a perfect mirror for the sensitivity rolloff
and axial resolutions sims.

iph1 = I1.*R; % Current at the 1st photodiode
iph2 = I2.*R; % Current at the 2nd photodiode

iph = (iph1-iph2); % Generated photocurrent

% Photodetector noise
nep = ((8e-12)*sqrt(B));
nep = wgn(1, length(iph), nep, 'linear', 'real');

% OCT signal w/ added noise
Vout = (iph*G) + nep;

% Low pass Butterworth amplifier - simulation of the frequency response of the balanced
detector
% Final signal
Iw = filter(Hd, Vout);
% Hd (cutoff freq 400Mhz) is  defined using fdatool

%% A-scan
FFT = (abs(fftshift(ifft(Iw))));
N = length(FFT);
Ascan = FFT(1, (N/2+1):N);
% Max = max(Ascan);
% Max = 20.*log10(Max); % For the sensitivity rolloff sims.

zz = linspace(0,(N*pi*c)/(2*1.*wwrange), length(Ascan)); % Spatial range
zz = zz./1e-3;
figure(), plot(zz, Ascan), title(‘A-scan'), xlabel('Depth (mm)')
ylabel('Amplitude (a.u.)')
```